Cover Letter

Plymouth, February 20th, 2020

Dear editor,

we herewith submit the revised version of our manuscript “Fluid-mediated, brittle-ductile deformation at seismogenic depth: Part II – Stress history and fluid pressure variations in a shear zone in a nuclear waste repository (Olkiluoto Island, Finland)”, with applied the requested minor corrections. We added UTM coordinates to the maps in Figure 1 and in the figure caption. We thank you for the rapid response to the revised manuscript, and we are appreciative for the recognition of our revision work.

Please address all the correspondence to:

Francesca Prando
PhD Student
Plymouth University, SoGEEs
B509, Portland Square, Drakes circus
PL48AA
E-mail: francesca.prando@plymouth.ac.uk

We look forward to hearing from you at your earliest convenience.

Best regards,
Francesca Prando, corresponding author.

Plymouth, February 10th, 2020

Dear editor,

We submit for your attention the revised version of our manuscript “Fluid-mediated, brittle-ductile deformation at seismogenic depth: Part II – Stress history and fluid pressure variations in a shear zone in a nuclear waste repository (Olkiluoto Island, Finland)”, hoping that you will find it sufficiently improved toward its publication in Solid Earth. The review process has highlighted the limitations of our proposed model, and helped us to sharpen our work and improve it in light of some constructive criticisms that were made by the reviewers.

In their comments the reviewers requested an improvement in the readability of the manuscript, specifically in regards to its length and structure. Other important points were made regarding (1) our interpretation of the temperature evolution of the fault zone in study, (2) the available constraints on the regional tectonic evolution of the study area, and (3) the limitations of the proposed conceptual model of the fault zone. Our detailed answers to each of these points were submitted during the open discussion, as a reply to the reviewers. Our answers had openly discussed each point and explained how we intended to implement the required changes in the amended version.

We present now the revised version, and to ease the progress in the revision procedure we will not repeat all the content of the initial rebuttals. We confirm here that we have changed the manuscript and the figures as per discussion.

To help you appreciate the revision work, we submit a version of the file in review mode, with all changes highlighted.

Hereby we sum up the main changes done with our revision work:

- We have shortened and restructured the manuscript by polishing the language and removing unnecessary text sections, as requested by both reviewers.

- The introductory sections (1-3) have been shortened retaining the key information relevant to our study. In particular section 2 (geological setting) focusses more on the Paleoproterozoic regional deformation history of Olkiluoto. Part of section 3 (methods) has been moved into the supplementary material.

- We restructured the results section presenting the microstructural observation (4.1- 4.2), eliminating the division between quartz and secondary mineral microstructures, to better explain why only quartz was then considered for EBSD analysis presented in section (4.3).

- We have modified some of the figures to better convey the text presented in the revised manuscript, specifically in the microstructural description (Fig. 3-5) and in the discussion (Fig. 12-13)

- The presentation of Temperature and Pressure constraints in section 4.5 has been modified in the light of the discussion occurred with both the reviewers. Tables T1 and T2 presenting the mineral chemistry data have also been modified.
- Following the recommendations of both reviewers, we simplified the discussion on the temperature estimate (5.1), and we emphasised the results obtained from the microstructural observations. We recognize the limitations of the T estimate in the cataclasite, and do not consider the results of our T estimate as sufficiently good to constrain the T of the final brittle deformation event. This has been discussed in the revised text.
- In section 5.2, we took into consideration the limits of the constraints available and improved the discussion on the possible causes of the observed increase in stress towards the shear zone centre.
- Following the recommendation of reviewer#2, we modified and simplified the discussion of the proposed model (section 5.3), introducing a new table (T3) instead of paragraphs on the text to present the parameters used for the model itself.

Please address all the correspondence to:

Francesca Prando
PhD Student
Plymouth University, SoGEEs
B509, Portland Square, Drakes circus
PL48AA
E-mail: francesca.prando@plymouth.ac.uk

We look forward to hearing from you at your earliest convenience.

Best regards,
Francesca Prando, corresponding author.

Fluid-mediated, brittle-ductile deformation at seismogenic depth: Part II – Stress history and fluid pressure variations in a shear zone in a nuclear waste repository (Olkiluoto Island, Finland)

Francesca Prando[1], Luca Menegon[1,2], Mark. W. Anderson[1], Barbara Marchesini[3], Jussi Mattila [4,5] and Giulio Viola[3]

[1] School of Geography, Earth and Environmental Sciences, University of Plymouth, PL48AA Plymouth, UK
[2]The Njord Centre, Department of Geoscience, University of Oslo, P.O. Box 1048 Blindern, Norway
[3]Dipartimento di Scienze Biologiche, Geologiche e Ambientali, Università di Bologna, Italy
[4] Geological Survey of Finland, Espoo, Finland
[5] Currently at: Rock Mechanics Consulting Finland Oy (RMCF), Vantaa, Finland

Correspondence to: Francesca Prando (francesca.prando@plymouth.ac.uk) and Luca Menegon (luca.menegon@plymouth.ac.uk)

Abstract. Microstructural record of fault rocks active at the brittle ductile transition zone (BDTZ) may retain information on the rheological parameters driving the switch in deformation mode, and on the role of stress and fluid pressure in controlling different fault slip behaviours. In this study we analysed the deformation microstructures of the strike-slip fault zone BFZ045 in Olkiluoto (SW Finland), located in the site of a deep geological repository for nuclear waste. We combined microstructural analysis, electron backscatter diffraction (EBSD), and mineral chemistry data to reconstruct the variations in pressure, temperature, fluid pressure and differential stress that mediated deformation and strain ~~localization~~localisation along BFZ045 across the BDTZ. BFZ045 exhibits a mixed ductile-brittle deformation, with a narrow (< 20 cm thick) brittle fault core with cataclasites and pseudotachylytes that overprint a wider (60-100 cm thick) quartz-rich mylonite. ~~Ductile~~ Mylonitic deformation took place at 400-500° C and 3-4 kbar, typical of the greenschist facies metamorphism at the base of the seismogenic crust. ~~Cataclastic deformation occurred under lower T conditions down to T ≥ 320° C and was not further overprinted by mylonitic creep.~~ We used the recrystallized grain size piezometry for quartz to document a progressive increase ~~in~~of differential stress ~~during mylonitization~~, from ca. 50 MPa to ca. 120 MPa~~. The increase in differential stress was localised,~~ towards the shear zone centre~~, which was eventually overprinted by brittle deformation in a narrowing shear zone.~~ during mylonitization and strain localisation. Synkinematic quartz veins ~~emplaced~~formed along the mylonitic foliation ~~during an early, low stress creep event, and were overprinted~~due to transiently high pore fluid pressure, up to lithostatic value. The overprint of the veins by dynamic recrystallization and mylonitic creep ~~at increasing differential stress~~is further evidence of the occurrence of brittle

events under overall ductile conditions. We propose a conceptual model in which the ductile-brittle deformation cycle was controlled by transient oscillations in fluid pressure ~~in a narrowing shear zone deforming at~~and progressively higher differential stress ~~during cooling~~, possibly occurring in a narrowing shear zone deforming towards the peak strength of the crust at the BDTZ.

1 Introduction

The change from fracturing and frictional sliding to dominant thermally activated creep processes accommodating viscous flow in mylonitic rocks occurs at the brittle–ductile transition zone (BDTZ; e.g. Kohlstedt et al., 1995; Handy et al., 2007). ~~Conventional strength envelopes localize the BDTZ at a depth of 10-15 km in the continental crust (Kohlstedt et al., 1995, Ranalli, 1997, Bos and Spiers, 2002), corresponding to the base of the seismogenic zone (Sibson, 1982).~~ Strength envelopes ~~also~~ predict that the BDTZ coincides with a peak strength in the crust~~,~~ at an approximate depth of 10-15 km between the brittle upper crust and the ductile middle- and lower crust. Naturally constrained stress profiles through exhumed mid-crustal rocks are consistent with this picture (Behr and Platt, 2011).

~~However, field evidence of seismic behaviour followed by solid-state viscous creep below the brittle-ductile transition in the continental crust (Austrheim, 2013, Menegon et al., 2017; White 1996, 2012), as well as of the cyclical interplay between brittle and ductile deformation~~ However, cyclical switches in deformation style during the evolution of mid-crustal shear zones (e.g. Pennacchioni and Mancktelow, 2007; Fusseis and Handy, 2008; Wehrens et al., 2016; Melosh et al., 2018)~~,~~ demonstrate that the BDTZ occupies a depth interval that can vary transiently, reflecting changes in, e.g., ~~stress and fluid pressure, as well as changes in shear zone- and fault microstructures (Handy et al., 2007). More specifically, different deformation mechanisms (dislocation creep, diffusion creep, fluid-assisted veining, dissolution-precipitation creep, fracturing and cataclasis) overlap in space and time at the BDTZ as a function of lithology, P-T conditions, and oscillating stress, strain rate and fluid pressure. Thus, the BDTZ occurs over a relatively wide range of conditions in a depth interval marked by significant fluctuations in strength~~bulk strength of the shear zones (Hirth and Tullis, 1994; Scholz, 1998; Fossen and Cavalcante, 2017; Melosh et al., 2018) and fluid pressure (Cox, 2010; Kjøll et al, 2015; Sibson and Rowland, 2003; Yardley and Baumgartner, 2007; Hirth and Beeler, 2015; Marchesini et al., 2019~~) that steer the overall short- and long-term rheological behaviour of the crust. Given that shear zones at the BDTZ act~~). Lithology, P-T conditions, as ~~rheologically weak detachment horizons within the crust (Handy and Brun, 2004; Gueydan et al., 2003; Pfiffner, 2016), understanding the effects of~~ well as variations in stress~~-~~, strain rate~~-~~ and fluid pressure ~~fluctuations on the rheological evolution of shear zones at the BDTZ is an~~are important ~~goal in tectonics research. In particular, it~~factors controlling the occurrence of different deformation mechanisms (dislocation creep, diffusion creep, fluid-assisted veining, dissolution-precipitation creep, fracturing and cataclasis) that overlap in space and time at the BDTZ. It is important to assess whether evidence of ~~such~~ cyclical fluctuations ~~are~~of those parameters is preserved in the geological record, and whether the extent of such variations can be estimated by examining natural fault rocks.

Microstructures can record crucial information on the parameters steering deformation ~~cycles~~ at the BDTZ, and are an invaluable tool that enables derivation of rheological parameters of shear zones (e.g. Stipp et al., 2002; Behr and Platt, 2011; Ceccato et al., 2018). However, the mutual overprinting relationships between brittle and ductile deformation and associated fault rocks at the BDTZ typically result in only partial microstructural records, in which the youngest deformation event might have completely overprinted the evidence of earlier deformation episodes. Recent deformation experiments have~~, however,~~ opened up new avenues for the ~~detailed~~ investigations of natural deformation microstructures in quartz-rich rocks that result from stress variations during brittle-ductile deformation. The 'kick and cook' experiments, for example, have documented quartz microstructures formed during transient high stress deformation followed by stress relaxation (Trepmann et al., ~~2007). Similar microstructures found in natural shear zones formed below the BDTZ were interpreted to results from seismic loading from the overlying brittle crust, followed by either static grain growth or dislocation creep deformation at relaxing stress (Trepmann and Stöckhert, 2003, 2013; Trepmann et al., 2017).~~2007). Deformation experiments conducted by Kidder et al. (2016) show that the microstructure associated with a stress increase in quartzite is a bimodal distribution of recrystallized grain size. The smaller grains accurately record the stress increase, whereas the surviving coarser grains formed during earlier, lower stress deformation. The smaller grains can be used to constrain differential stresses during the most recent (high stress) deformation event using a recrystallized grain size palaeopiezometer (Stipp and Tullis, 2003; Cross et al., 2017).

Fluids can also play a fundamental role in triggering a transient switch from dominantly ductile to brittle deformation, as demonstrated, for example, by the synkinematic emplacement of quartz veins subsequently overprinted by crystal-plastic deformation (Handy et al., 2007; Kjøll et al., 2015; Trepmann and Seybold 2019; Marchesini et al., 2019). Cyclical ductile-brittle-ductile deformation associated with high fluid fluxes involving a fault-valve behaviour (Sibson, 1990) implies cycles of fluid pressure build-up followed by fluid venting and pressure drop, and has been related to seismic fault behaviour (Sibson, 1992; Cox, 1995; Nguyen at al., 1998; Viola et al., 2006). ~~Near lithostatic values of fluid pressure are required to facilitate synkinematic vein emplacement in a shear zone at the BDTZ (Cox, 1995; Streit and Cox, 2001; Cox, 2007; Hirth and Beeler, 2015).~~

~~Given the fundamental interplay between variations in P-T conditions, fluid pressures, stress and strain rate occurring at the BDTZ, f~~Fault modelling and field studies must attempt to quantify the thermal and structural history of fault rocks, as well as the fluid activity in faults ~~in order~~ to ~~untangle~~identify the ~~relative contribution of different rheological~~ parameters ~~in~~ controlling the dominant deformation mode and mechanisms active at seismogenic depths. This study investigates the microstructural record of the deformation behaviour at the BDTZ of a subvertical sinistral strike-slip fault hosted in ~~granitoids~~the basement of the Paleoproterozoic Baltic Shield in Finland. The fault occurs within the deep ONKALO spent nuclear fuel repository that is currently being built on the island of Olkiluoto in SW Finland (Fig. 1a). The present-day structure of the fault consists of a narrow (< 20 cm thick) brittle fault zone core that ~~exploits~~is contained inside a ~~wider (ca.~~thicker (max 1 m thick) ductile, mylonitic ~~precursor~~shear zone. We constrain the deformation history of the fault zone and use quartz microstructure to estimate the stress history of the mylonitic precursor. We propose a conceptual model of the evolution of fault slip behaviour that incorporates the constraints on differential stress and fluid pressure derived from our microstructural analysis, and that ~~favours the scenario of~~applies to a narrowing shear zone that progressively ~~localizes~~localises strain when deforming across the BDTZ.

2 Geological Setting

~~-~~The island of Olkiluoto in SW Finland (Fig. 1a) is ~~located in the Paleoproterozoic bedrock~~part of the Paleoproterozoic Baltic ~~shield. The region is dominated by high-grade metasediments and by plutonic rocks, emplaced~~Shield, which was consolidated during the latest accretionary stages of the Svecofennian Orogeny between ca.1.89 and 1.80 Ga (Lahtinen et al 1994, Nironen et al. 1997, Lahtinen et al 2005, Pajunen et al. 2008). In the study area, the dominant rock types consist of amphibolite facies migmatitic metasediments~~, calc-alkaline synorogenic TTG-type granitoids, and late-orogenic leucogranites and pegmatites. The migmatisation occurred~~ formed between ca.1.84-1.82 Ga~~ (Aaltonen et al. 2016), during the collisional stage of the Svecofennian Orogeny characterized by considerable crustal thickening and high-grade metamorphism (Kukkonen and Lauri, 2009). Stable mineral assemblages constrain the formation of the migmatite~~, at 3.7-4.2 ~~Kbar~~kbar and 660-700° C (Tuisku and Karki, 2010~~). Tonalite and granodiorite intrusions were emplaced prior to the metamorphic peak, between ~~, Aaltonen et al. 2016), ca. 1.89 and 1.85 Ma old calc-alkaline synorogenic TTG-type granitoids that~~1.89 and 1.85 Ma~~ predate the migmatisation (Mänttäri et al., 2006), ~~while leucogranites intrusions emplaced during the high-grade metamorphism~~ and syn- to late~~-~~-orogenic ~~stages, between~~leucogranites and pegmatites intruded ca. 1.85 to 1.79 Ga (Mänttäri et al., 2010). ~~Retrograde~~Following the peak metamorphism leading to migmatisation, retrograde metamorphism under greenschist facies conditions affected the ~~rocks soon after the peak conditions,~~area and continued throughout the subsequent orogenic collapse, dated at ca.1.79-1.77 Ga for SW Finland (Lahtinen et al., 2005). ~~Approximately 150 Ma later, during an extensional tectonic phase, Southern Finland was intruded by Rapakivi granites (1.65-1.54 Ga), with the Laitila and Eurajoki plutons located at 15 and 4 km eastern of Olkiluoto, respectively. Crustal extension also caused the formation of an NW–SE trending graben 50 km north of Olkiluoto, later filled with Mesoproterozoic sandstones. Olkiluoto bedrock was affected by the emplacement of NE-SW striking diabase dykes (1.56 Ga) and Greisen veins associated with the Rapakivi batholiths intrusions and graben formation. The intrusion of olivine diabase sills occurred during a phase of regional compression at c. 1.27-1.25 Ga (Suominen 1991).~~

~~The study area was affected by a polyphase~~ Polyphase ductile deformation affected Olkiluoto between ~1.86 and 1.79 Ga (Aaltonen et al., 2016), followed by a ~~complex~~polyphase brittle deformation history~~, as a result of exhumation and cooling. Aaltonen et al. (2010)~~ between ~1.75 to 0.8 (Mattila and Viola, 2014). Field studies identified characteristic structures for three (D_2-D_4) deformation stages, which overprint a pre-migmatite, poorly preserved deformation stage (D_1~~). At 1.86-1.83 Ga, D_2 deformation affected progressively the bedrock of Olkiluoto, developing a pervasive~~; Aaltonen et al. 2010, and references therein). Deformation during D2 (~ 1.86-1.83 Ga) and D3 (~1.83 to 1.81 Ga) occurred under amphibolite facies condition; D_2 developed a penetrative NE-SW striking high-grade (locally migmatitic) foliation dipping moderately towards SE, as well as NE–SW striking mesoscopic shear zones~~ (Aaltonen et al. 2010). The following D_3 stage (1.83 to 1.81 Ga) was more localized and occurred under amphibolite facies conditions. It resulted in NNE-SSW striking foliations, observed in the central part of~~

~~Olkiluoto~~. D$_3$ developed a more localized NNE-SSW striking foliations, and E-W to NE-SW trending, S to SE dipping shear zones (Aaltonen at al. 2010). The latest stage, D$_4$, developed under greenschist facies retrograde metamorphism around ~1.81–1.79 Ga according to U/Pb dating of syn-kinematic pegmatites (Mänttäri et al., 2010). D$_4$ structures consist of NNE-SSW and N-S striking subvertical ductile shear zones, varying in ~~width~~thickness from ~ 0.5 m to 200 m (Fig.1a).

~~The progressive regional exhumation led to a switch in deformation style, with the onset of brittle deformation in Olkiluoto at ~ 1.75 Ga (Mattila and Viola, 2014, Aaltonen et al., 2016). Mattila and Viola (2014) used paleostress inversion of fault slip data to identify seven distinct brittle stages that developed in the time span from 1.75 to 0.8 Ga. These brittle deformation stages are characterized by both~~Brittle deformation in Olkiluoto was characterized both by the reactivation of optimally oriented pre-existing ductile structures, and by the formation of new Andersonian-type faults and joints. The dominant brittle structures ~~in the study area~~ can be grouped into two main sets: (1) an E-W to NE-SW trending set of low angle faults exploiting the D$_2$ regional migmatitic foliation, and (2) a set of subvertical faults striking N-S to NW-SE (Fig. 1; Aaltonen et al., 2016). ~~We assumed that, previous~~Paleostress inversion of fault slip data permitted to ~~the~~identify seven distinct brittle ~~stage, the crust in Olkiluoto had been passively exhumed~~ stages during the ~~late- to post-orogenic deformation stages of the Svecofennian orogeny (Lahtinen et al., 2005). Low angle faults cross-cut the subvertical faults and attest to a later stage~~Paleoproterozoic-Mesoproterozoic structural history of ~~exhumation (Aaltonen et al., 2016).~~

~~The subvertical faults have orientation compatible with~~SW Finland (Mattila and Viola, 2014). Of interest for this study is the first ~~stage of~~ brittle deformation ~~identified by Mattila and Viola (2014), and they typically form~~stage that developed conjugate systems of NNW–SSE sinistral and NW–SE dextral strike-slip faults ~~(Mattila and Viola, 2014). This conjugate system has been interpreted to result from~~, in accordance with the NW–SE to NNW–SSE compression proposed for the late- to post-Svecofennian orogeny (Viola et al., 2009; Torvela and Ehlers, 2010; Saintot at al., 2011). Field observations indicate that faults optimally oriented for the first stage of brittle deformation commonly exploit NNE-SSW and N-S precursor shear zones charactereistic of the D4 stage of ductile deformation (Aaltoonen et al, 2016; Nordbäck et al., 2018; Skyttä and Torvela, 2018). A network of vertical N-S and NW-SE faults has been mapped and investigated at the repository scale in Onkalo with underground surveys and boreholes (Aaltonen et al. 2016, Fig 1b). N-S faults are typically ~~localized~~localised on mica-rich precursor ductile shear zones (Pere, 2009). The role of subvertical, N-S striking ductile precursor zones in controlling the ~~localization~~localisation of faults at the disposal site was investigated by Skyttä and Torvela (2018), who identified the ductile precursor structures as short limbs of D$_4$ asymmetric folds and as anastomosing networks of discrete retrograde (greenschist facies) ductile shear zones. Skyttä and Torvela (2018) proposed that the subvertical N-S faults formed as a result of progressive strain localisation during the late stage of D$_4$ ~~deformation~~, which culminated in the development of discrete faults through linkage of individual fault segments that preferentially exploited optimally oriented branches of the anastomosing network of localised ductile ~~high strain~~shear zones. ~~As such~~Therefore, the faults exploiting D$_4$ shear zones represent ideal targets to investigate the deformation processes and mechanisms at the brittle-ductile transition in Olkiluoto, and the associated rheological parameters recorded in the fault rock microstructures. This study uses the N-S sinistral strike-slip fault BFZ045 as a natural laboratory to investigate the stress history of the ductile precursor and the possible role of fluids on the deformation processes active at the brittle-ductile transition. The companion paper by Marchesini et al. (2019) has thoroughly described the deformation history of the conjugate ~~(yet very different)~~ dextral BFZ300 fault.

3 Methods

3.1 Sampling

Samples were obtained from two sub-horizontal drill cores from the underground facilities that intersect the BFZ045 fault (Fig. 2a). The analysed samples were selected from (i) a 2 m continuous section along drill core PH28, which was drilled at a depth of 433 m b.s.l. and is oriented ESE-WNW, and (ii) drill core PH16 from the Demonstration Facilities tunnels at 420 m depth, described in Aaltonen et al. (2016). The PH28 samples were selected from the 99-~~101m~~101 m interval of the drill core, with core distance measured from ESE to WNW, which includes the fault core and the proximal damage zone. ~~The~~The selected interval of the drill core was cut in half parallel to the stretching lineation and perpendicular to the mylonitic foliation and subsampled at regular intervals of 2 cm. Nineteen polished thin sections ~~cut parallel to the stretching lineation~~ were added to three samples from PH16 previously described in Aaltonen et al. (2016). An additional thin section from drill core PH21 (drilled at the same depth of PH16) was used to estimate the T of the ~~fabric~~graphite formation in the host rock using Raman spectroscopy of carbonaceous material (see 3.3~~2~~ and 4.5).

3.~~1~~2 Microstructural observations and Electron Backscatter Diffraction (EBSD) analysis

Deformation microstructures were ~~investigated~~studied using petrographic ~~microscopy~~ and scanning electron microscopy (SEM). SEM and EBSD analysis ~~was~~were performed at the Plymouth University Electron Microscopy Centre using a JEOL LV6610 SEM and a JEOL 7001 FEG-SEM. Thin sections used for Electron Backscatter Diffraction (EBSD) analysis were polished with colloidal silica before being carbon coated. Data were acquired on a NordlysNano and a NordlysMax EBSD detector (Oxford Instruments). Working conditions during acquisition of the EBSD patterns were 20 kV, 20 mm working distance, 70° sample tilt and high vacuum. AZtec software was used for pattern indexing on rectangular grids with step size of 0.7 µm, 1 µm and 1.8 µm. EBSD patterns were processed with the Channel 5 software (Oxford Instruments), and noise reduction was performed following the procedure suggested in Bestmann and Prior (2003). ~~The EBSD data are presented as grain size maps, with a 10° misorientation threshold to define grain boundaries (in black), while low-angle boundaries are defined as having misorientation > 2° and < 10° and are displayed as white or cyan lines. The grain size was measured as the diameter of a circle with equivalent area to the grain. The spread of the internal orientation of each grain was shown as Grain Orientation Spread (GOS) maps and was considered as a measure of the internal strain of the grain. A trade-off curve was used to calculate a threshold GOS value, which separates recrystallized grains from relict grains, following the procedure outlined in Cross et al. (2017). The average recrystallized grain size, calculated as root mean square (RMS), was used to apply the EBSD calibrated recrystallized grain size piezometer for quartz (Cross et al., 2017). Grain reference orientation deviation angle~~

~~maps (GROD) were used to visualise subgrains only partially outlined by low-angle boundaries and to estimate their size. GROD maps are colour coded to show the angular deviation at each point of a grain from the average orientation of the grain. Quartz c-axis orientation is presented as pole figures on equal area, lower hemisphere projections, and one point per grain. The XY plane of the pole figure is parallel to the shear zone foliation, X is parallel to the stretching lineation, and Z is normal to the foliation.~~

Differential stresses during mylonitic creep were estimated using the recrystallized grain size piezometer for quartz of Cross et al. (2017). The method relies on the separation between relict and recrystallized grains based on the Grain Orientation Spread (GOS), which is a measure of the internal strain of a grain defined as the average misorientation angle between each pixel in a grain and that grain's mean orientation (Wright et al., 2011).Further details on the presentation of the EBSD data and on the recrystallized grain size piezometer for quartz of Cross e al.(2017) are presented in the supplementary material (S1).

3.~~2~~3 Mineral chemistry and Raman spectroscopy

~~A first semi-quantitative chemical composition point analysis was conducted using a JEOL 7001 FEG-SEM equipped with energy-dispersive spectrometer (EDS) at the Electron Microscopy Centre of the University of Plymouth.~~ Major element mineral chemistry of chlorite and white mica was measured with Electron Microprobe Analysis (EMPA), at the Department of Earth Sciences, University of Milan, Italy. Carbon coated thin sections were probed with a JEOL 8200 Super Probe equipped with 5 wavelength-dispersive spectrometer (WDS). Working conditions were set to 15 kV of probe current, 5nA current on sample, 1 µm beam diameter. Natural minerals were used for standardization, measurement times were 30s on peaks and 10s on backgrounds of the X-ray lines.

Raman spectroscopy was applied for feldspar and opaque phase identification and for carbonaceous material (CM) characterization. Data acquisition was conducted at the Department of Chemistry, University of Padua (Italy), using a Thermo Scientific DXR MicroRaman spectrometer, equipped with a 532 nm depolarised laser. Raman analysis was also carried out at the Department of Mathematical, Physical and Computer Sciences of the University of Parma (Italy) using a Jobin-Yvon Horiba LabRam spectrometer equipped with He–Ne laser (emission line 473.1 nm) and motorized XY stage. Spectra were acquired from polished thin section, using a laser power of 5 mW, spectrograph aperture 25 µm pinhole, and ~~a~~ 50X or50X low distance objective. The estimate spot size was 1.~~1~~-2 µm in diameter and spectral resolution of 2 to 4.4 cm^{-1}, with acquisition time of 30–90 s. Feldspars composition was classified on the basis of the acquired Raman spectra, as suggested in Freeman et al. (2008), using a comparison with standard Raman spectra from the RRUFF Project database (Lafuente et al. 2015). To assure a good statistical analysis of the CM structural heterogeneity, only samples with > 10 CM spectra were taken in consideration. Omnic software (Thermo Fisher Scientific) was used for Raman spectrum decomposition, using the software Lorentian/Gaussian function, following the procedure described in Koeketsu et al. (2009). ~~A linear relationship between temperature and the Raman parameter R2 (derived from the area of the defect band relative to the ordered graphite band) forms the basis of the CM geothermometer (Beyssac et al., 2002). Temperature can be estimated to ± 50 °C in the range 330–650 °C. Deformation can affect the internal disorder and underestimate the temperature obtained from the spectra analysis (Kirilova~~

~~et al., 2017). To consider the possible role of deformation, analysis of CM both in the host rock and along the D_4 mylonitic foliation were collected. Care was taken to avoid CM within cracks, and to prevent altered measurement from CM damaged during the thin section polishing, we performed measurements by focusing the laser beam on CM beneath the surface of a transparent adjacent grain as suggested in Beyssac et al. (2002).~~Raman analytical conditions are detailed reported in the supplementary material (S1). A discussion about the analytical limitation of the chosen methods for temperature estimation is also presented in S1.

4 Results

4.1 BFZ045 fault zone structure

~~Underground field observations and measurements indicate that~~ A schematic representation of BFZ045 ~~is a strike-slip~~ fault~~,~~ ~~with an average orientation of 87/095 (dip/dip direction,~~ geometry obtained from underground field mapping and detailed characterization along the horizontal PH28 drill core is represented in Fig. ~~2b) and with a mixed ductile-brittle deformation style that manifests itself as a~~2a. A 10-100 cm wide mylonite with a sinistral sense of shear, ~~overprinted by~~oriented 61/075 (dip/dip direction), hosts a sub-vertical network of cohesive cataclasites~~, fault breccias cemented by~~ with an average orientation of 87/095 (Fig. 2b). Rodding of quartz~~, chlorite and sulphides, and by a network of veins typically filled with chlorite, quartz, and calcite.~~ and feldspar in the mylonite defines a stretching lineation oriented 10/168 (plunge/trend; Fig. 2b,c). Slickensides with chlorite mineral striations are abundant throughout BFZ045 and the average orientation of the striations is 07/169 ~~(plunge/trend, Fig. 2e). Stepped~~; stepped slickensides indicate a dominant sinistral sense of shear, although striations associated with dextral kinematics have also been observed~~. The damage zone is typically 0-5 m thick and is characterized by an increased fracture density towards the fault core. Fractures are mostly filled by chlorite (Aaltonen et al, 2016~~ (Aaltoonen et al. 2016; Nordbäck et al., 2018).

~~The structure~~A network of veins typically filled with chlorite, quartz and calcite, and chlorite filled fractures overprint the mylonite and host rock (Fig 2a; Aaltonen et al, 2016). The damage zone is localised between 0.5 to 1 m from the fault ~~rocks of BFZ045 were~~ core, and is characterized ~~in detail from the two cores PH28 and PH16, both drilled approximately at~~by an increased fracture density towards the ~~depth of 420 meters. The horizontal drill core PH28 provides a cross section of BFZ045, where a 2 m thick damage zone surrounds a 60 cm thick~~ fault core, with the average spacing between fractures decreasing from 3 cm to ca. 0.5 cm. ~~characterised by a sub-vertical network of~~With the term "fault core", we refer here to the brittle core of BFZ045 defined by cohesive cataclasites ~~and veins~~ that overprint ~~a mylonite oriented 61/075 (dip/dip direction, Figs. 2a, b, d). A schematic representation of the fault geometry along PH28 is represented~~the mylonite. This means that the damage zone of BFZ045 affects both the migmatitic host rock and the BFZ045 mylonite.

In figure 2d, representative samples of core PH28 are shown from left to right in a sequence from the damage zone in ~~Fig. 2a.~~the host rock to the fault core. The host rock is a coarse-grained veined migmatite ~~consisting of 40 vol% of quartz, 50 vol% of feldspars, and 10 vol% of muscovite~~ (Fig. 2d, I).

~~The damage zone of BFZ045 consists of an asymmetrical (~20 cm east side of the core and ~ 60 cm on the west side) fractured host rock surrounding a mylonitic fault core (Fig 2a). Its boundaries were~~The extent of damage in the host rock was defined by the farthest occurrence of chlorite filled fractures, identified microscopically as deformation ~~band as they are~~bands associated with visible slip. A total of 12 fractures longer than 5 cm ~~were~~can be observed along the core, of which 7 within a distance of 10 cm from the fault core (west side of the core). ~~Fracture density increases towards the contact with the brittle fault core, with the average spacing between fractures decreasing from 3 cm to ca.~~ The contact between the host rock and the mylonite is sharp. ~~0.5 cm. Chlorite and calcite are the most common minerals partially filling the fractures oriented variably with respect to the mylonitic foliation. The contact between the damage zone and the mylonite is sharp.~~

The millimetre-spaced mylonitic foliation is defined by a compositional layering of alternating ~~quartz-feldspathic~~quartzofeldspathic domains and mica-rich domains (Fig. ~~2b~~2d, II).~~ Rodding of quartz and feldspar defines a stretching lineation, with average orientation of 10/168 (plunge/trend) (Fig. 2b,c).~~ Multiple slip surfaces marked by 0.5 – 10 cm thick cataclastic domains overprint the mylonite along the foliation (Fig. 2d, III). Locally, phyllosilicates and trails of opaque minerals define thin (<~~1mm~~1 mm thick) anastomosing foliation planes within the cataclasites, which wrap around sub-angular fragments of the mylonitic precursor. Along a thin (<5 mm thick) slip surface, two pseudotachylyte injection veins intruding the mylonite at a high angle have been observed, which demonstrates the transient seismogenic behaviour of BFZ045(white arrow in Fig. 2d,III). ~~The pseudotachylyte main generation surface is less than 1 mm thick and is parallel to the mylonitic foliation (Fig. 3c).~~ Calcite veins (1-3 mm thick) locally overprint the fault core ~~either~~both at high angle to the foliation ~~or~~and along the slip surfaces~~. Representative micrographs of samples taken from the fault core and from its damage zone are shown in figure 3~~.

4.2 ~~Microstructures~~Petrography and ~~petrography~~microstructures

4.2.1 Host rock

The migmatitic host rock mineral assemblage observed in the PH28 samples consists of 50 % of quartz~~ (qtz),~~, 40 % K-feldspar ~~(kf),~~, and plagioclase~~ (pl),~~ and the remaining 10% of white mica~~ (wm),~~, graphite, alteration minerals of plagioclase (sericite) and secondary chlorite, and calcite veins. Coarse-grained (1-~~2mm~~2 mm) quartz and feldspars are homogeneously distributed in an equigranular texture and show mostly straight grain boundaries~~.~~ (Fig. 3a). K-feldspar occurs as orthoclase, with a well-developed veined perthitic texture. Plagioclase, albitic in composition as determined from Raman analysis, has lamellar twinning and is commonly altered ~~into~~to sericite. Both types of feldspar locally show bent twin lamellae and undulose extinction. ~~White mica was observed occasionally as millimetric sub-euhedral grains.~~

~~The damage zone retains the same mineral assemblage of the host rock, except along the chlorite filled shear bands and fractures (Fig 3a). Shear bands appear as cohesive micro-cataclasites, with fine grained (< 10 µm) chlorite surrounding angular feldspar and quartz clasts. Calcite veins are preferentially oriented at high angle to the mylonitic foliation (60° to 85°).~~

Microfractures in feldspars are preferentially oriented parallel and at low angle (≤ 20°) to the ~~foliation. Both orientations correspond to the orientation of fluid inclusion trails observed in quartz (section 4.3.1).~~

mylonitic foliation.White mica was observed occasionally as millimetric sub-euhedral grains.~~The relative mineral abundances in the mylonite are slightly different from those in the host rock, and consist of 50% quartz, 20% white mica + chlorite, and 30% K-feldspar + plagioclase. Accessory phases are rutile, anatase, and apatite, which are typically found associated with chlorite to form black seams. The spaced mylonitic foliation is defined by a compositional banding between alternating millimetre-thick quartz bands and narrower (0.2 to 1 mm thick) mica- and feldspars-rich bands (Fig. 3b). Porphyroclasts of K-feldspar are up to 7 mm in size and show asymmetric pressure shadows filled with chlorite + muscovite ± feldspars (albite and K-feldspar), with a geometry indicative of a sinistral sense of shear. Veins of radiate chlorite are observed cutting the mylonitic foliation at a high angle (~60°).~~

~~The brittle overprint in the fault core occurs mostly as 3 to 10 cm thick protocataclasites, with chlorite rich C' shear bands cutting the mylonitic foliation and indicative of a sinistral sense of shears. The protocataclasite transitions to 0.5 - 2 cm thick cataclasite bands in the fault core. Compared to the host rock the cataclasite bands are richer in chlorite and opaque minerals, which occur as fine-grained (2-10 µm) flaky aggregates within the quartz + feldspars + muscovite rich matrix. Clasts are predominantly angular fragments of the mylonite, ranging in size from 100 µm to 5 mm, and surrounded by a variable proportion of fine grained (<50 µm) matrix (Fig. 3c). Foliation in the matrix is defined by aligned phyllosilicates and anastomosing dark seams of opaque minerals. Veins with radiate chlorite that typically overprint the mylonite were also observed within mylonitic clasts inside the cataclasite.~~

~~A fine grained pseudotachylyte generation surface is observed subparallel to a cataclastic band (Fig. 3c), identified from characteristic centimetric injection veins, branching in the mylonitic rock at high angle to the foliation. The matrix of the pseudotachylyte is completely altered to a fine-grained, <2 µm, chlorite and muscovite rich matrix that surrounds survivor clasts of quartz and rutile (Fig. 3d).~~

~~In the following section, we present a detailed description of quartz deformation and recrystallisation microstructures in the mylonite and in the cataclasite. We used the varying deformation microstructure of quartz as a proxy for the variation of differential stress and fluid pressure during the deformation of BFZ045 at the brittle-ductile transition.~~

~~4.3 Quartz microstructures~~

~~4.3.1 Damage zone~~

~~The damaged host rock shows large sub-euhedral quartz grains (> 3mm) with lobate to straight grain boundaries.~~ Quartz displays intracrystalline deformation features such as undulatory extinction, wide extinction bands (WEBs, following the terminology of Derez et al., 2015; Fig. ~~4a~~3b), and bulges resulting in sutured grain boundaries (Fig. ~~4b~~3c; Stipp and Kunze, 2008). WEBs are locally bounded by fluid inclusion trails with different orientations, which give them a blocky or slightly elongated aspect (Figs. ~~4a-b~~3b-c). Two main sets of intracrystalline fluid inclusion trails are observed, one at a low angle with respect to the mylonitic foliation and the other perpendicular to the foliation. Fine bulges (10-20 μm in size) occur along grain boundaries and intercrystalline fractures (Fig. ~~4a~~3b). Quartz grains in the proximity of the mylonite (sample PH28-2, Fig. 2b) develop intracrystalline bands of recrystallized grains sub- parallel to the foliation, with grain size of ~ 30-60 μm (Fig. 3c). Shear bands in the deformed host rock appear as cohesive micro-cataclasites, with fine grained (< 10 μm) chlorite surrounding angular feldspar and quartz clasts.

4.~~3.~~2 ~~Fault core~~ .2 Mylonite

Formatted: Heading 1

The relative mineral abundances in the mylonite are slightly different from those in the host rock, and consist of 50% quartz, 20% white mica + chlorite, and 30% K-feldspar + plagioclase. Accessory phases are graphite,rutile, anatase, and apatite, which are typically found associated with chlorite to form black seams. The spaced mylonitic foliation is defined by a compositional layering between alternating millimetre-thick quartz bands and narrower (0.2 to 1 mm thick) mica- and feldspars-rich bands (Fig. 4a). Porphyroclasts of K-feldspar are up to 7 mm in size and show asymmetric pressure shadows filled with chlorite + muscovite ± feldspars (albite and K-feldspar), with a geometry indicative of a sinistral sense of shear. Feldspars in the mylonite present brittle behaviour, with domino-type fragmented porphyroclasts Neoblasts of feldspar are commonly observed in the pressure shadows of phorphyroclasts or toghether with fine-grained white micas along the mylonitic foliation.

Quartz in the mylonite presents various degrees of recrystallization (Figs. ~~5a~~ 4b, c). In zones where ductile deformation is less prominent (e.g. samples PH28_3, PH16_1, Fig. 2), quartz retains a coarser grain size (1-5 mm), and forms slightly asymmetric (sigmoidal-shaped) grains. Internally, the grains display patchy undulatory extinction, well-developed blocky to elongated WEBs (100-300 μm wide), and discrete intracrystalline bands (< 200 μm wide) of bulges and recrystallized grains preferentially oriented sub-parallel to the foliation and at ca. 45° from the foliation, measured anti-clockwise (Fig. ~~5a~~4b). The host grains contain small subgrains (< ~~60μm~~60 μm), which, towards the boundaries of the host grain, make transition to aggregates of recrystallized grains of size comparable to the subgrains, forming typical core-and-mantle microstructures (Fig. ~~5a~~4b).

In zones of complete recrystallization ~~at a distance >2 cm from the cataclastic fault zone core~~, quartz forms highly elongated polycrystalline ribbons (up to 0.5 – 1 mm thick, and up to 2 cm long) parallel to the foliation (Fig. ~~5b~~4c). The recrystallized grains locally define a shape preferred orientation (SPO in Fig. ~~5b~~4c) inclined with 10° to 30° with respect to the trace of the foliation, consistently with the bulk sinistral sense of shear.

Adjacent to the cataclastic ~~unit, at a distance < 1 cm~~fault core (sample PH16_3, Fig. 2), ataxial/unitaxial (i.e. with no visible median line; Bons, 2012) quartz veins ~~are observed (Fig. 5c). They~~ occur parallel to the mylonitic foliation (and to the layers of recrystallized quartz) and contain grains elongated normal to the vein boundary (i.e. normal to the foliation; Fig. 4d). The vein crystals range in length from 200-400 μm and have a maximum thickness of 150 μm measured parallel to the vein. Quartz in the veins shows undulatory extinction and bulges at the grain boundaries (Fig. ~~5d~~4e) indicative of crystal plastic deformation. The recrystallized quartz in the mylonite surrounding the vein has a finer grain size than the one in the mylonite described in

Figs. ~~5a-b~~4a-c, which is located farther away from the cataclastic core. Veins of radiate chlorite are observed cutting the mylonitic foliation at a high angle (~60°).

4.2.3 Cataclasite

The brittle overprint in BFZ045 occurs mostly as 3 to 10 cm thick protocataclasites, that ~~The protocataclasite~~ transitions to 0.5 - 2 cm thick cataclasite bands in the fault core.

~~Quartz in the mylonite at distances < 2 cm from the cataclasites~~The cataclasite is rich in chlorite and opaque minerals, which occur as fine-grained (2-10 µm) flaky aggregates within the fine grained (< 50 µm) quartz + feldspars + muscovite rich matrix. Locally, the cataclasite matrix contains a foliation defined by aligned phyllosilicates and anastomosing dark seams of opaque minerals. Clasts are predominantly angular fragments of the mylonite, ranging in size from 100 µm to 5 mm, and surrounded by a variable proportion of matrix (Figs. 3a-c). Quartz in the protocataclaste occurs in almost entirely recrystallized ribbons with a finer grain size (ca. 10 µm) than the one observed at higher distances from the brittle fault core (~~Fig.~~ Figs. 5b-c vs Figs. 4b-c).~~5e).~~ The quartz clasts in the cataclasite (Fig. ~~5f~~5c) preserve the deformation and recrystallization microstructures observed in the mylonite in close proximity to the cataclasite (Fig. ~~5e~~5b).

A pseudotachylyte generation surface is observed subparallel to a cataclastic band (Fig. 5a), and is identified from characteristic centimetric injection veins, branching in the mylonite at high angle to the foliation. The pseudotachylyte main generation surface is less than 1 mm thick and is parallel to the mylonitic foliation (Figs. 5a, d). The matrix of the pseudotachylyte is completely altered to a fine-grained, < 2 µm, chlorite and muscovite rich matrix that surrounds survivor clasts of quartz and rutile (Fig. 5d). Chlorite- and quartz aggregates commonly fill fractures within feldspar porphyroclasts in the mylonite. Similar fractured feldspar porphyroclasts with quartz + chlorite fillings are observed inside slightly rotated clasts of mylonite in the protocataclasites (Fig. 5e).

4.~~4~~3 EBSD and grain size analysis of quartz

4.~~4~~3.1 Mylonite

EBSD analysis of the mylonite was conducted on sample PH16_1, which is located at the mylonitic shear zone boundary at a distance of 4 cm from the brittle fault core (Fig. 2a). EBSD maps were acquired from intracrystalline bands of recrystallized grains within an elongated mm- sized quartz grain (Fig. 6a), and from a highly recrystallized quartz layer along the mylonitic foliation (Fig. 7a).

The recrystallized grain size within the intracrystalline bands ranges from 5 to 60 µm (Fig. 6b, c). The Grain Orientation Spread (GOS) within the recrystallized bands varies between 0° and 8.4°, with a threshold value of 1° between the recrystallized grains and the relict grains when analysing the trade-off curve proposed by Cross et al. (2017). The average grain size of recrystallized grains (GOS < 1°) is 16 ± 7 µm whereas relict grains (GOS > 1°) have an average grain size of 25 ± 9 µm. Relict grains contain subgrains of an average size of 17 ± 7 µm (Fig. 6f).

Quartz grain hosting the intracrystalline band shows subgrains of approximately 25-50 µm in size, which is comparable to the size of the coarser recrystallized grains observed in the intracrystalline bands (Fig. 6c). The size of the subgrains in the host quartz was estimated visually with the aid of Grain Relative Orientation Distribution maps (GROD, Fig. 6g).

In the recrystallized quartz layer (Fig. 7a), quartz grain shape ranges from equant to elongate parallel to the foliation, with grain size ranging from 5 to 87 µm (Figs. 7b, c). ~~Grain Orientation Spread (~~GOS analysis identified a threshold value of 1.56° to separate recrystallized- and relict grains (Fig. 7d). Average grain size of the recrystallized grains is 18 ± 8 µm, while relict grains have an average size of 28 ± 11 µm (Fig. 7e).

The relict grains contain subgrains of an average size of 17 ± 7 µm (Figs. 7c, f). The crystallographic preferred orientation (CPO) of the c-axis of the relict grains and recrystallized grains forms a single girdle consistently inclined with the sinistral sense of shear of the sample (Fig. 7g). The EBSD-calibrated recrystallized grain size piezometer for quartz of Cross et al. (2017) was used to estimate the differential stresses during plastic flow in the mylonite. The estimated differential stress is 73-80 MPa for the average recrystallized grain size of 16-18 µm.

4.~~4~~3.2 ~~Vein~~Veins parallel to the mylonitic foliation

The quartz vein parallel to the foliation shown in Fig. 5c and 8a was analysed to identify possible evidence of crystal-plastic deformation and dynamic recrystallization. Grain shape varies from fibrous with elongation perpendicular to the vein wall, to more equant/less elongate. Grain boundaries of vein crystals are straight to lobate, the latter most commonly observed in association with fine recrystallized grains and bulges (< 15 µm in size) (Figs. 8 b, c). Irrespective of their shape, most of the grains contain low-angle boundaries and Dauphiné twins. The low-angle boundaries are typically arranged to define polygonal to slightly elongated domains of ~10 µm in size, comparable to that of the surrounding recrystallized grains in the mylonite (Fig 8c).

Quartz in the mylonite flanking the vein shows fine grain size (< 20 µm), with only a small fraction of coarser grains (30-60 µm). ~~Grain Orientation Spread (~~GOS~~)~~ analysis indicates that dynamic recrystallization is pervasive. The mean recrystallized grain size is 10 ± 3 µm, and the relict average grain size is 20 ± 9 µm, with a GOS threshold value of 1.94° (Figs. 8d, e). Selected relict grains (size > 40 µm) in the mylonite contain subgrains with size between 5 to 25 µm range (Fig. 8f). Finer grains observed within the vein also present a GOS value below the threshold, which suggests they represent the recrystallized fraction in the quartz vein (Figs. 8c, f). In the vein quartz, GOS analysis indicates that the average subgrain size is 24 ± 7 µm, although the largest fraction of subgrains is smaller than 15 µm, i.e., similar in size to the recrystallized grains in the flanking mylonite and in the vein itself. The c-axis CPO of the recrystallized grains in the mylonite forms a single girdle synthetically inclined with the sinistral sense of shear (Fig. 8h). The c-axis CPO of recrystallized grains in the veins overlaps with the one of the relict grains (Fig. 8i). The differential stress estimated from the average recrystallized grain size in the mylonite (10 µm) is 106 MPa.

4.~~4~~3.3 Cataclasite

We analysed a largely recrystallized quartz clast in the cataclasite from sample PH28_10 (Fig. 9a). The selected clast is rotated of less than 10° with respect to the adjacent mylonitic foliation. Quartz grain size in the clast ranges from 4 to 60 µm. The coarser grains are elongated parallel to the foliation, show bulges and fine recrystallized grains at their boundaries, and contain a high density of low-angle boundaries (Fig. 9b). The low-angle boundaries define small polygonal domains of a size comparable to the one of the recrystallized grains found at the grain boundaries (Fig. 9c). The GOS map in figure 9d identifies two grain size distributions, separated by a GOS threshold value of 3.23°. The recrystallized grains (average grain size: 8 ± 4 µm) form equigranular aggregates at the boundaries of the coarser (average grain size: 17 ± 10 µm) elongated relict grains. The c-axis CPO of the recrystallized grains and of the relict grains is the same, showing two maxima at an intermediate position between the centre of the pole figure and its periphery, and consistently inclined with the sinistral sense of shear of the sample (Fig. 9f). The differential stress estimated from the average recrystallized grain size in the clast (8 µm) is 123 MPa. Although the map has been acquired from a clast, these microstructures and recrystallized grain size are ~~representative~~similar to those of the mylonite in the immediate vicinity (< 2 cm) of the brittle fault core (Figs. ~~5e, f~~5b, c).

4.~~5~~4. Mineral chemistry, Raman spectroscopy, and pressure-temperature (P-T) conditions of deformation

We estimated the P-T conditions of mylonitic~~ and cataclastic~~ deformation using Raman spectroscopy of carbonaceous material (RSCM), chlorite thermometry, and phengite barometry. Carbonaceous material was observed as grains and aggregates ranging in size from ~ 50 to ~ 200 µm in the host rock (sample PH21_1, Fig. 10a) and as smaller grains (20~~-~~–50 µm) along the mylonitic foliation~~,~~ (sample PH16_1-2, Fig. 10b~~)~~), along chlorite and muscovite rich layers. Data of Raman peaks deconvolution are reported in the Supplementary Material (S1). We estimated a ~~peak metamorphic~~maximum temperature of 530~~°±~~° C ± 50° C for the carbonaceous material in the host rock (Fig. 11a) (using the thermometer calibration for a laser wavelength of 514 nm, Beyssac et al. 2002), and a lower T of ~~436°~~440° C ± 50° C for the mylonite (Aoya et al., 2010, using the thermometer calibration for a laser wavelength of 532 nm~~) (~~; Fig. 11a). ~~The average~~The pressure during mylonitization was estimated using the Si-in-phengite geobarometer (Massonne and Schreyer, 1987). Representative compositions of white mica are listed in Table 1. The full dataset of chemical compositions of white micas is reported in the Supplementary Material (S1). White mica composition was measured for grains parallel to the foliation associated with ~~stable~~ neoblasts of K-feldspar, as the application of the Si-in-phengite geobarometer requires stability of K-feldspar (Figs. 10c, d~~) and structural~~). Structural formulae were calculated assuming 11 oxygens. The range of Si apfu in the probed ~~muscovite~~white mica grains is 3.12 –3.16. This compositional range indicates a pressure of 2-4 ~~Kbar using~~kbar for the ~~Si-in-phengite geobarometer~~mylonitization (Fig. 11b~~, Massonne and Schreyer, 1987),~~), considering the average temperature of 440° C derived for the mylonite with the graphite thermometry.

Chlorite composition was determined for i) chlorite grains intergrown with quartz and muscovite in the strain shadows around feldspar porphyroclasts in the mylonite (Fig. 10c, d), ii) chlorites flakes aggregate in the cataclasite quartz matrix (Fig. 10e), and iii) radiate chlorites filling veins at high angle to the mylonitic foliation (Fig. 10f). The structural formula of chlorite was calculated based on 14 oxygens, and representative composition are shown in Table 2. The full dataset of chemical compositions for chlorite is reported in the Supplementary Material (S2).

Chlorites along the mylonitic foliation ~~and in the cataclasite~~ have ~~similar~~ Si content ~~(~~(~2.~~54~~60 - 2.~~75~~70 apfu), Al between 2.~~48-~~74-2.~~82~~88 apfu, and are moderately Fe-rich with a XFe (XFe=Fe/(Fe+Mg)) between 0.62 and 0.82. Chlorites in the mylonitic sample from PH_16 have a more narrow range of XFe, between 0.~~55~~57 and 0.~~6.~~73(see supplementary material S1) .In the cataclasite chlorites Si content range between 2.53-2.772 apfu, and Al have a wider range of 2.61-2.94 apfu (S1). The cataclastic chlorite is richer in Fe compared to the mylonite, with a XFe range between 0.71-0.85. The radial chlorite filling the veins cutting the mylonite has Si content between 2.51 and 2.780 apfu, Al between 2.74 and 3.00 apfu, and ~~smaller~~ XFe ~~variations, between~~variationsbetween 0.69 and 0.81. In general, BFZ045 chlorites have a aphrosiderite-ripidolite composition and the microprobe results show that the composition of distinct chlorite generations is similar (Fig. 11c). The CHL(2) semi-empirical thermometer of Lanari et al. (2014) was applied to each EMPA analysis of chlorite with Si~~<~~ < 3 apfu and (Na + K + Ca) < 0.1apfu. FeO was used as Fe total, and a_{H2O}~~=~~ = 1 and a_{SiO2}~~=~~ = 1 were assumed. The estimated temperature for the mylonite ranges from ~380 ~~°~~° C to 500 ~~°~~° C (limit of the used thermometer~~), with an average T of 440 °C~~) for an assumed P of 3.5 kbar (Fig. ~~11d). Mean temperatures~~11d), with a temperature variation of 10° C every 0.5 kbar increment. Temperatures estimated for the cataclasite matrix ~~(414 °C)~~ and for the radiated chlorite in the veins ~~(424 °C) are slightly lower than those of the mylonite, and compositions~~have a larger range (~300-500° C, Fig 11d). Compositions yielding T lower than 400 ~~°~~° C are more frequent, especially in the cataclasite ~~(Fig 11d). The estimated temperature varied by 10 °C every 0.5 kbar increment.~~, however no clear relationship could be discerned between temperature and microstructural position of the chlorites.

5. Discussion

Our observations constrain the details of the structure and the deformation history of BFZ045. In particular, the microstructures of fault rocks indicate a sequence of deformation events where ductile deformation (mylonitisation) was punctuated by brittle deformation (veining), and eventually culminated in the formation of the brittle, cataclastic fault core. We interpret this sequence to result from the evolving stress history and possible fluid pressure variations ~~along~~during the ~~fault. In the following, we discuss the constraints provided by our microstructural analysis, and derive a conceptual model~~overall ductile-to-brittle deformation history of ~~fault~~ the strike-slip ~~behaviour of~~ BFZ045 ~~at the brittle-ductile transition.~~ fault.

5.1 The sequence of deformation events in BFZ045: ductile-brittle deformation ~~cycles in the middle crust~~history

Our microstructural observations are consistent with the general conclusion that brittle deformation along BFZ045 exploited a ductile (mylonitic) precursor (Nordbäck and Mattila al., 2018; Skytta and Torvela, 2018). Veins, cataclasites and pseudotachylytes are localised along the mylonitic fabric of BFZ045, and only minor evidence of brittle deformation (mostly

Formatted: Subscript

Formatted: Subscript

in the form of fractures filled by chlorite) is present outside of the mylonitic fault core (Figs. 2a, 3a). ~~The analysed samples document a switch from dominant ductile to brittle deformation mode, via a transitional deformation stage where overall ductile conditions were punctuated by veining.~~

The first stage of deformation of BFZ045 is represented by the development of a ~~localized~~localised N-S trending mylonitic foliation ~~in the migmatites~~ (Figs. 2, ~~3b, 5a, 5b~~4a-c). Mylonitic creep was punctuated by transient brittle events, with the opening of extensional fractures along the mylonitic foliation filled by quartz veins (Figs. ~~5c,~~4 d,e). Veining was again followed by mylonitic deformation, as indicated by dislocation creep and dynamic recrystallization microstructures of quartz in the veins. Mylonite and veins were then overprinted by brittle deformation that formed cm- thick cataclasites (Figs. ~~3c, 5e, 5f~~5a-c) and a < 0.5 cm thick pseudotachylyte (Fig. 5d) that, together, form the brittle fault core of BFZ045. ~~The pseudotachylyte is recognizable from injection vein intruding the~~Cataclasites and pseudotachylytes were not overprinted by mylonitic ~~precursor (Fig. 3c,d).~~ creep, which might indicate that they formed under condition favourable to predominantly brittle deformation along BFZ045. The observed parallelism between stretching lineation in the mylonite and chlorite slickenlines in the cataclasites ~~indicates~~suggest that the ductile-brittle deformation history of BFZ045 occurred under a ~~constant~~prolonged strike-slip regime with sinistral kinematics~~, as shown by the kinematic indicators in the mylonites and by the stepped slickensides observed in the field.~~ (Figs.2b,c). This conclusion is consistent with the model of the brittle evolution of SW Finland proposed by Mattila and Viola (2014), which attributes the sinistral kinematics of NNW-SSE trending subvertical faults to the ductile-brittle transition stage of the basement at 1.75 Ga (~~stage~~Stage 1 of deformation in Mattila and Viola, 2014). BFZ045 experienced later reactivations during the prolonged brittle history of the SW Finland basement, as indicated by calcite veins cutting the brittle fault core and by (rare) slickenlines with dextral kinematics observed in the underground exposures (Aaltonen et al. 2016). Local dextral kinematics along BFZ045 is potentially consistent with the ~~stage~~Stage 2 of deformation of Mattila and Viola (2014) at 1.7-1.6 Ga. These later features, however, are not discussed further in this paper as they are subordinate to, and did not obliterate the earlier history.

~~The sequence of deformation events recorded along BFZ045 is estimated to have occurred in the middle crust under slightly decreasing T from 450-500 °C to 320-400 °C (Fig. 11). We note that cataclasites and pseudotachylytes are not overprinted by mylonitic creep, which might indicate that they formed when the temperature was sufficiently low to favour predominantly brittle deformation along BFZ045.~~

~~A temperature of 440 ± 50 °C is derived from graphite thermometry along the mylonitic foliation, which is approximately 100° degrees lower than the T of 530 ± 50 °C estimated from the graphite thermometry in the host rock fabric (Fig. 11a). This is consistent with the retrograded greenschist facies conditions attributed to the final stages of D4 deformation in the SW Finland basement at 1.81-1.77 Ga (Lahtinen et al., 2005; Mänttäri et al., 2010). If the graphite analysed in BFZ045 represents carbonaceous material that was mobilized after the D2-D3 deformation phases that formed the main foliation in the host rock, then the T of 440 ± 50 °C indicates the T of graphite crystallization during the D4 greenschist facies metamorphic overprint and mylonitization of BFZ045. However, the difference in temperature between the host rock fabric and the shear zone can~~

~~also be explained as the result of strain-induced disorder in the crystal lattice of the analysed graphite, which might result in an underestimation of the temperature of formation of the graphite (Kirilova et al., 2018). Considering the 50° error range of the thermometer and the difference in estimate due to the use of two different calibrations that for the same R2 values can determine different temperatures (Fig. 12c) (Beyssac et al. 2002; Aoya et al. 2010), a temperature estimate of 440 ± 50 °C for the mylonite is acceptable.~~

~~A T of 440° was considered to constrain the P at the time of deformation along BFZ045 using the phengite geobarometer (Massonne et al, 1987) (Fig. 12d). The peak metamorphic temperatures obtained from the mylonite suggest a P of 3-4 kbar, which overlaps with the P estimates based on stable mineral assemblages of Tuisku et al. (2010) of 3.7 – 4.2 kbar at the culmination of regional metamorphism in Olkiluoto (phase D_2-D_3). We interpret this result as representative of the conditions during mylonitic deformation along BFZ045 in the middle crust after peak metamorphism.~~

~~Our estimate of P-T conditions of mylonitization of BFZ045 (~450 °C, 3-3.5 kbar) are consistent with the late Svecofennian orogeny and the emplacement and cooling of pegmatitic granites in SW Finland (Aaltonen et al. 2010). The pegmatitic granites emplaced at 15-12 km depth, were then affected by the last stage of ductile deformation D_4 and cooled below 300 °C ca. 1.75 Ga ago (Aaltonen et al. 2010).~~

~~Our results indicate that the T ranges derived from chlorite thermometry in the mylonite and in veins cutting the mylonitic foliation overlap (Fig. 12d), with only a few analyses in the veins yielding T < 400°C. This overlap suggests that chlorite veining occurred early in the deformation history of BFZ045 (i.e. at T ≥ 450°C) and that it continued during decreasing T. Constraining the T of formation of cataclasites is more difficult, because the chlorite grains might be fragments of the mylonitic chlorite. However, we only probed flake chlorite aggregate comparable to radiated chlorite in the cataclasite and we consider the radiate morphology as indicative of growth within the cataclasite (Fig. 10e). Thus, although we cannot rule out that a few of the probed grains were fragments, our results indicate that the cataclasite formed at T ≥ 320 °C and potentially as high as 450-500 °C. The lowest T estimate from chlorite thermometry (300-320 °C) is derived from a few grains in the cataclasite and in the vein (Fig. 11d), and still locates the observed deformation activity in the middle crust at T ≥ 300°C.This is consistent with the results of Marchesini et al. (2019), who estimated a minimum T of 350°C for the early stages of deformation and emplacement of quartz veins along the dextral fault zone BFZ300 (conjugate to BFZ045). Considering an average P of 3.5 kbar during ductile-brittle deformation along BFZ045 and an average crustal density of 2.7 g/cm3, the depth of deformation corresponds to approximately 13 km, which is consistent with the depth typically considered as representative of the base of the seismogenic crust at the BDTZ (e.g. Scholz, 1990, Kohlstedt et al., 1995). We note that our P estimate is valid only for the mylonitic creep stage of the deformation history of BFZ045, as no suitable geobarometer was found in the cataclasite.~~

Formatted: Affiliation, Line spacing: 1.5 lines

5.2 Deformation mechanisms and stress history during mylonitic creep of BFZ045

~~5.2 Interpretation of quartz microstructures: stress history during mylonitic creep of BFZ045~~

Microstructural observations show that ~~quartz in~~ductile deformation of the mylonite BFZ045 ~~mylonitic core~~was accommodated ~~deformation~~in quartz by dislocation creep~~. The most common~~, while feldspars experienced dominantly brittle behaviour with only limited neocrystallization in pressure shadows (Figs. 10c). Given the lack of crystal plastic deformation and recovery features in the interior of feldspar porphyroclasts, we interpret the neocrystallization in pressure shadows as a possible indication of dissolution-precipitation, which has been commonly reported in feldspars deforming at mid-crustal conditions (Fitz Gerald and Stünitz 1993; Menegon et al. 2008; Eberlei et al., 2014; Torgersen et al., 2015; Giuntoli et al., 2018; Hentschel et al., 2019).

Quartz recrystallization microstructures (bulges at~~ the~~ grain boundaries and within intracrystalline bands, and core and mantle microstructures with subgrains of comparable size to that of the recrystallized grains~~:~~; Figs. 4, 5) suggest that bulging and subgrain rotation were the dominant recrystallization mechanisms (Hirth and Tullis, 1992; Stipp and Kunze, 2008). The average recrystallized grain size ~~in all our samples falls within the range where bulging,~~ of quartz ranges between 8 and 18 µm, which falls whitin the < 40 µm size value representative of bulging as dominant recrystallization mechanism (defined as slow grain boundary migration coupled to localised subgrain rotation at the mantle of the host grain~~, is expected to be the dominant recrystallization mechanism (~~; Stipp et al., 2010). ~~Our microstructural observations and EBSD maps are consistent with this.~~

~~The average recrystallized grain size of quartz decreases from the mylonitic shear zone boundary (16-18 µm) towards to shear zones centre (8-12 µm), which has been overprinted by the brittle fault zone core (Fig. 12).~~ In all the ~~areas investigated with EBSD, we regularly observed~~studied samples, GOS analysis distinguished two quartz grain size populations~~ of grains~~, in which the coarser (relict) grain size contains subgrains of size comparable to the average ~~grain~~ size of the finer recrystallized grains (Figs. 7-~~10~~9). The CPO of relict and recrystallized grains is the same, and this is consistent with the host-controlled development of a CPO during subgrain rotation recrystallization (e.g. Stünitz et al. 2003). ~~Despite the slight differences in CPO patterns between the individual analysed sites (Figs. 8-10), the key observation is that the CPO of both the coarse (16-18 µm in samples PH16_1) and the fine (8-12 µm in samples PH16_3 and PH28_10) recrystallized grain size fraction is consistently inclined with the sinistral sense of shear of the samples. We interpret the consistent sinistral asymmetry of the quartz c-axis CPOs as strong evidence that the different recrystallized grain size fractions all developed during sinistral strike-slip ductile activity of BFZ045. Thus, the grain size variations, and in particular the fine recrystallized grain size observed in samples PH16_3 and PH28_10, are interpreted to result from the stress history during mylonitic deformation of BFZ045, and not from discrete events of late reactivation and overprint of the fabric.~~

~~We interpret~~A key observation in the BFZ045 mylonite is the decrease in recrystallized grain size of quartz from the shear zone boundary (16-18 µm~~ as representative of the long term ‘steady state’ mylonitic flow of BFZ045 at a differential stress of 73-80 MPa. Such~~) towards the centre (8-12 µm; Fig.7-9). The coarser (16-18 µm) grain size is the most representative of the partially- (Fig. 7) and of the nearly completely (Fig. 8) recrystallized quartz ribbons in the BFZ045 mylonite at distances ≥ 4 cm from the brittle fault core, and it also occurs as relict grain size in quartz clasts embedded in the cataclasite, where it is overprinted by the finer (8-12 μm) recrystallized grains (Fig. 10). ~~It is worth noting that quartz~~ We interpret this overprint and the overall decrease in ~~the mylonite in close proximity~~ recrystallized grain size to ~~the cataclasite, as well as in clasts within~~reflect a progressive increase in stress and strain rate towards the ~~cataclastite (~~shear zone centre during mylonitic creep (Kidder et al. 2016). Troughout the samples ~~PH28_7-10 and PH16_3 in Fig. 2), systematically exhibits a large number~~the CPO of recrystallized ~~grains belonging to the finer population (8-12 μm, Figs.~~ quartz is consistently inclined with a sinistral sense of shear (Fig. 6-9~~, 10). This overprint is~~); this is interpreted as ~~the~~ evidence ~~of a local increase in stress (up to 120 MPa) during mylonitic creep (Kidder et al. 2016). The average recrystallized grain size of 16-18 μm is associated with relict~~that they developed under constant kinematic conditions in BFZ045.

Relict quartz grains of 25-28 μm in size are associated with the coarser (16-18 μm) grain size (Figs. 7-8), and un-recrystallized portions of quartz contain subgrains of similar size (≥ 25 μm, Figs. 7b-d). We ~~speculate~~consider that the 25-28 μm grain size population might represent an early,~~ lower stress (i.e. around 50-60 MPa)~~ dynamic recrystallization event within BFZ045, which was later overprinted by recrystallization occurring under progressively increasing differential stress.

Deformation and stress history of BFZ045 can be summarised in different stages. After the regional metamorphic peak and migmatite formation (i.e. 660-700° C, 3.7-4.2 kbar; Tuisku and Lauri, 2009), the basement of Olkiluoto was affected by different stages of ductile deformation (D_2-D_4, Aaltonen et al., 2010) under a metamorphic retrograde path toward greenschist facies conditions. The progressive change in P-T condition was favourable to the mobilization and subsequent recrystallization of carbonaceous material (e.g. Kirilova et al., ~~Our discussion of the stress history of BFZ045 relies on the GOS method to separate between relict and recrystallized grains. It is known that the GOS method has a slight grain size bias, which results in higher GOS values for larger grains (Cross et al., 2017). However, this bias has no impact on the ability to separate between relict and recrystallized grains where their size overlaps on the cumulative grain size distribution, and the GOS-based separation is considered robust (Cross et al., 2017). One key observation that supports our GOS-based separation is that relict grains systematically contain subgrains of the same size of the new, finer recrystallized grains. Thus, we are confident that our analysis has reliably identified different recrystallized grain sizes.~~

~~In summary, the differential stresses estimated from the different populations of recrystallized quartz grains increase from 73-80 MPa to a peak value of 120 MPa towards the contact with the cataclasite. An earlier, lower stress (ca.54 MPa) deformation is possibly recorded in the (few) relict quartz grains of 25-28 μm that contain subgrains of around 17 μm of average size (Figs. 7, 8). We are aware of the uncertainties and limitations of the palaeopiezometric calibrations, and our estimated flow stresses must be taken with care. However, we consider the systematic decrease in recrystallised grain size towards the cataclastic fault core to be meaningful and to reflect a change in the rheological conditions during mylonitic creep. Given the similar T conditions across the studied profile, we conclude that this change reflects an increase in stress and strain rate. To explain this increase in stress and strain rate towards the shear zone centre, we discuss two possibilities:~~

~~(1) Increasing stress and strain rate towards the brittle shear zone centre may reflect the rheological evolution of a shear zone that is narrowing with progressive exhumation from the ductile to the brittle crust. In such a model, the peak stress conditions~~

Formatted: Subscript

Formatted: Subscript

~~are reached at the brittle-ductile transition under progressively decreasing T (e.g.~~ 2017). We thus interpret the estimated metamorphic temperature of 530° C ± 50° C in the host rock as the temperature of remobilization of carbonaceous material durin retrograde metamorphism that culminated in the D_4 deformation stage. During the final stage of D_4 a localised N-S trending mylonitic foliation developed in the migmatites (Fig. 12a). Mylonitic creep took place under differential stresses increasing from ~ 54 to ~ 80 MPa, as determined from the recrystallized grain size of 16-18 µm overprinting grains of 25-28 µm. Foliation-parallel quartz veins crystallized transiently along the mylonitc foliation (Fig. 12b) and were overprinted by crystal plastic deformation and dynamic recrystallization under progressively higher stress (80-120 MPa, Figs. 8, 12c) during strain localisation towards the center of the shear zone. We are aware of the uncertainties and limitations of the palaeopiezometric calibrations, and our estimated flow stresses must be taken with care. However, the similarity between subgrain- and grain size, as well as the consistent sinistral asymmetry of the quartz c-axis CPO of relict and recrystallized grains in all the maps support that dynamic recrystallization occurred during the sinistral strike-slip movement of BFZ045 under progressively increasing differential stresses.

We estimate that mylonitization of BFZ045 (Fig. 12a-c) occurred at ~450° C and 3.5 kbar, consistent with the retrograde greenschist facies conditions attributed to the final stages of D_4 deformation in the SW Finland basement at 1.81-1.77 Ga (Lahtinen et al., 2005; Mänttäri et al., 2010; Skytta and Torvela, 2018). Considering an average crustal density of 2.7 g/cm^3, the depth of mylonitic deformation and of transient veining in BFZ045 corresponds to approximately 13 km.

The mylonite and quartz veins were eventually overprinted by more pervasive brittle deformation that formed chlorite veins, cm-thick cataclasites and a < 0.5 cm thick pseudotachylyte that, together, form the brittle fault core of BFZ045 (Fig. 12 d). We attempted to estimate the temperature of chlorite veins cutting the mylonitic foliation and of chlorite in the cataclastic matrix (Fig. 11), but we obtained a wide temperature range of ~300-500° C that is unable to constrain the precise T of the final brittle deformation event(s). Although the conditions of formation of cataclasites and pseudotachylytes cannot be tightly constrained, it is interesting to note that the T estimates from the chlorite in the veins are generally higher than 400° C. This suggests that chlorite veining occurred early in the deformation history of BFZ045 (i.e. at T ≥ 400° C) under overall ductile conditions, as also supported by the precipitation of chlorite + quartz aggregates in microveins and in strain shadows (Fig. 5e). This is consistent with the results of Marchesini et al. (2019), who estimated a temperature of at least 350° C for the early stages of deformation and emplacement of quartz-chlorite veins along the dextral fault zone BFZ300 (conjugate to BFZ045). ~~Kohlstedt et al., 1995; Behr and Platt, 2011). The results of our chlorite thermometry study support this model, as they are consistent with an overall T decrease from 450-500 °C to 320 °C during protracted mylonitic creep followed by a cataclastic overprint along the brittle fault core. In this scenario, BFZ045 would represent a case of narrowing shear zone that evolved from a distributed- to a progressively more localised ductile deformation and eventually brittle deformation during cooling and exhumation (type II shear zone of Fossen, 2017). During this evolution, dislocation creep and fluid-assisted veining occurred simultaneously, as expected in the 270-350° C temperature range considered typical of the frictional-viscous transition in quartz-rich rocks (Dunlap et al., 1997; Handy et al., 1999; Stöckhert et al., 1999; Stipp et al., 2002). Our work is unable to constrain the amount of exhumation associated with the cooling and progressive localization in the brittle fault core, as the~~

~~strike-slip nature of BFZ045 cannot be responsible of significant exhumation. Considering a transpressional regional tectonic regime during the sinistral strike-slip activity of BFZ045 (stage 1 of deformation in Mattila and Viola, 2014), we speculate that the combination between thrusting and erosion was the main exhumation process of the Olkiluoto basement at around 1.75 Ga. In this scenario, BFZ045 was active within the Olkiluoto basement while it was being passively exhumed. However, we emphasize that a detailed appraisal of the mechanisms responsible of the passive exhumation of the Olkiluoto basement is beyond the scope of this study. Kärki and Paulamäki (2006) estimated a regional geothermal gradient of ca. 40 °C km^{-1} during retrogressive metamorphic conditions that culminated in the post-D_4 exhumation of the Olkiluoto basement. Assuming a regional geothermal gradient of ca. 40 °C km^{-1}, mylonitic deformation of BFZ045 at 440-500 °C would have occurred at ca. 11-12 km depth, whereas cataclastic deformation at 320-400 °C at 8-9 km depth.~~

~~(2) Alternatively, and assuming that the cataclasite formed at similar T (and depth) of the mylonite (T ≥ 400 °C), the increase in stress recorded by the finer recrystallized grain size might be attributed to external stress loading from seismic faulting in the overlying upper crust (i.e. seismic loading) (e.g. Küster and Stöckhert, 1998; Trepmann and Stöckhert, 2003; Trepmann et al., 2017; Trepmann and Seybold, 2019). The presence of pseudotachylytes along the BFZ045 fault core indicates that the fault was capable of generating earthquakes, and the seismogenic behaviour of other faults in the Olkiluoto basement has been previously discussed (Marchesini et al., 2019 and refs. therein). Thus, local high differential stresses in the BFZ045 mylonites could had been induced by seismic activity in the overlying upper crust. However, the fine-grained recrystallized fraction is exclusively localised in the immediate vicinity of the brittle fault core of BFZ045, whereas in case of earthquake-induced stress variations a more diffuse overprint within the entire width of the shear zone (and perhaps even outside of it) would be expected. Dislocation glide-controlled deformation microstructures of quartz typically interpreted as the evidence of seismic loading in the ductile crust, such as conjugate micro-shear zones, short wavelength undulatory extinction, and sub-basal deformation lamellae (Trepmann and Stöckert, 2013; Trepmann et al., 2017) have not been observed in the mylonite and in the damage zone of BFZ045 (Figs. 3-5). Furthermore, cataclasites and pseudotachylytes are not mylonitised, and this is consistent with overall decreasing temperature conditions that inhibited the efficiency of thermally activated creep processes. Thus, we favour the model whereby the documented decrease in the recrystallized grain size of quartz towards the BFZ045 fault core reflects the rheological evolution of a narrowing shear zone, which reached peak stress conditions at the BDTZ.~~

5.3 Conceptual model of the fault slip behaviour of BFZ045 at the base of the seismogenic zone

~~In order to estimate the relative contributions of variations in fluid pressure and differential stress in facilitating different fault slip behaviours, we modelled a possible failure mode evolution of BFZ045 using the λ-σ failure~~

Using a λ-σ failure mode diagram (Cox, 2010), ~~with the following assumptions and using the following parameters:~~

~~- We assumed~~we propose a ~~strike-slip Andersonian regime of faulting, according to the deformation history proposed by Mattila and Viola (2014). This is consistent with the dominant strike-slip stretching lineations and slickenlines observed on the core samples. In a strike-slip regime, the vertical stress is σ2, which we assume to correspond to the lithostatic load during deformation. This was estimated at 300-350 MPa during mylonitic creep from the phengite barometer. The maximum differential stress during stage 1 and stage 2 was considered to be in the range between 55 and 60 MPa, whereas during stage~~

Formatted: Font: Bold

Formatted: Normal

~~3 and stage 3 to stage 4 transition we consider a differential stress increasing progressively from 73 to 123 MPa. σ1 and σ3 values were calculated for a stress ratio R of 0.3 estimated by Mattila and Viola (2014) for the N-S sinistral faults in Olkiluoto. R is defined as R= σ2- σ3/ σ1- σ3~~

~~Strain rate during mylonitic creep was calculated~~ conceptual model of the structural evolution of BFZ045 (Fig. 13). Strain rates during mylonitc creep were estimated using the dislocation creep flow ~~law~~laws of ~~quartzite Eq. (1):~~

~~$\dot{\varepsilon} = A\sigma^{n} f_{H2O}^{m} \exp(-Q/RT)$~~

~~(1)~~

~~where $\dot{\varepsilon}$ is the strain rate, A an empirical constant, σ the differential stress, n the stress exponent, f_{H2O} the water fugacity, m the water fugacity exponent, Q the activation energy, R the gas constant, and T the temperature. Using the flow law for wet quartzite~~quartz of Hirth et al. (2001~~), we estimated the following strain rates during mylonitic creep: $\dot{\varepsilon}$ = 4.3 x 10^{-13} s^{-1} (for a differential stress of 50 MPa during stage 1), $\dot{\varepsilon}$ = 1.1 x 10^{-12} s^{-1} (for a differential stress of 73-80 MPa at the beginning of stage 3), and $\dot{\varepsilon}$ =6.9 x 10^{-12} s^{-1} (for the peak stress conditions during stage 3). Water fugacity was calculated with Wither's fugacity calculator based on Pitzer and Sterner (1994) equation of state for 450º and 3.5 Kbar (water fugacity exponent m = 1 in Hirth et al., 2001).~~

~~We assumed that viscous creep in the mylonite occurred at fluid pressure conditions higher than hydrostatic (λ=0.6), based on the Pf > 210 MPa proposed by Marchesini et al. (2019) for brittle failure under overall ductile conditions of the conjugate fault BFZ300.~~

~~Failure envelope for λ -σ failure mode diagrams were calculated using a friction coefficient λ of 0.6 (common value for granitoids, e.g. Sibson 1985), a cohesive strength of 26 MPa and a tensile strength of 13 MPa, which were taken from tensile strength measurements of granitic gneisses of Olkiluoto (Aaltonen et al., 2010).~~

~~Figure 13 shows the resulting model: stage 1 to stage 3 are representative of the deformation under ductile conditions, while stage 4 represents the final transition to brittle deformation. Failure~~). Parameters and assumptions used for the calculation of the strain rates and of the λ-σ failure envelopes ~~were calculated for progressively shallower depths (Figs. 13c, d)~~are listed in ~~order to account for the progressive exhumation discussed in section 5.2. BFZ045 was initially undergoing ductile deformation at differential stress < 60 MPa and a strain rate of ca. 10^{-13} s^{-1} (Fig. 13a, stage 1), developing a 25-28 µm recrystallized fraction.~~ Table 3.

According to the failure envelope, ~~low~~ differential stresses ~~(<80MPa~~ 80 MPa~~)~~ are necessary for extensional- and hybrid fractures to occur~~, therefore the emplacement~~. In our model, this stage of fault evolution is represented by the ~ 54 MPa creep recorded by quartz grain- and subgrain size of ~~the foliation-parallel veins (Fig.~~ 25-28 µm (Figs. 7b-d). The failure envelope also shows that extensional failure and vein formation required transient high fluid pressure reaching lithostatic values (λ = 1; Fig. 13b, stage 2~~) must predate the development of the finest recrystallized fractions developed under peak values (ca. 120MPa)~~

~~of differential stress. While the foliation-parallel veins are consistent with mode I opening mode due to hydrofracturing,~~). Although the overall geometric stress conditions during ductile deformation of BFZ045 are expected to generate en-echelon vein systems oblique to the mylonitic foliation~~. Thus, a transient reorientation of the stress field in the fault zone must be invoked to explain,~~ the foliation-parallel veins ~~during stage 2~~are consistent with mode I opening mode due to hydrofracturing. A regional rotation of the stress field appears unlikely, given the constant orientation of the stretching lineation and slickenlines in the core samples, and the consistent asymmetry of the pre- and post-vein quartz c-axis CPO (Figs. 7-9). Thus, a transient reorientation of the stress field in the fault zone must be invoked to explain the switch from viscous creep to mode I fracturing along the mylonite foliation.

~~Transient high fluid pressure reaching lithostatic values (λ = 1) during low-differential stress mylonitic creep was necessary to trigger a change in the deformation behaviour, with a switch from viscous creep to mode I fracturing along the mylonite foliation resulting in the emplacement of quartz veins (Fig. 13b, stage 2). The average subgrain size within the vein quartz is 24 µm (although the larger fraction is represented by subgrains smaller than 15 µm), which is similar to the population of the coarser recrystallized grains in the mylonite (Fig. 7). This might indicate that the quartz vein emplaced during an overall low differential stress creep event, which was later overprinted by progressively higher stress deformation as indicated by the subgrains < 15 µm in size and by the average recrystallized grain size of 12 µm both inside the vein and in the surrounding quartz-rich mylonite.~~

Veining was then followed by a ~~drop~~decrease in fluid pressure (e.g. Sibson, 1989, 1993; Cox 1995) and a switch back to mylonitic creep ~~(Fig. 13c, stage 3)~~ under progressively higher stress ~~conditions in a narrowing shear zone during slight cooling and exhumation (Fig. 13c, stage 3). Peak stress conditions recorded in the recrystallized grain size of quartz were reached in a highly localized shear zone at the fault core and corresponded to ca. 120 MPa (peak stress and~~ and strain rate ~~during stage 3, Fig. 13c). Cataclasites and pseudotachylytes overprinted this localised shear zone and formed the brittle fault core of BFZ045 (Fig. 13d, stage 4). In order to meet the brittle shear~~ conditions (Fig. 13c, stage 3). The failure ~~criterion, high values of~~ mode diagram indicates that these higher stresses are expected to result in brittle shear failure mode of the fault for a pore fluid pressure ~~(~~factor λ > 0.~~75) is required at the peak stress of ca. 120MPa, but we cannot rule out that shear failure occurred by a combination of increase in fluid pressure and differential stress after mylonitic creep had ceased (Fig. 13d). Any potential increase of stress beyond the ca. 120 MPa estimated from the~~ 8 ~~µm recrystallized grain size cannot be captured by our microstructural analysis. We must note that the actual path of variation of pore fluid pressure from stage 2 to stage 4 is not known, and we have no control on the extent of drop of pore fluid pressure after stage 2 (i.e., we do not know the value of λ during stage 3 mylonitic creep and prior to~~. The cataclasite and pseudotachylytes in the brittle fault core likely represent the final product of BFZ045 deformation under progressively higher differential stresses and fluid pressure across the BDTZ. However, the time span between the high strain rate mylonitic creep and the formation ~~in stage 4).~~

~~In summary, we propose the following conceptual~~ of the brittle fault core is unknown, and so are the exact P-T conditions of cataclasites and pseudotachylytes. Thus, our model for ~~the deformation history and the fault slip behaviour of BFZ045 in the Olkiluoto metamorphic basement (Fig. 13):~~stage 3 remains somewhat speculative.

The increase in stress towards the shear zone centre (Fig. 12c) may reflect the rheological evolution of a shear zone that is narrowing with exhumation under progressively decreasing T from the ductile to the brittle crust (e.g. Kohlstedt et al., 1995; Behr and Platt, 2011). Alternatively, it might be attributed to external stress loading from seismic faulting in the overlying upper crust (i.e. seismic loading; e.g.

~~1. Stage 1 is represented by long-term mylonitic creep along a N-S trending shear zone (Fig. 13a);~~

~~2. Mylonitic creep was punctuated by the emplacement of foliation-parallel quartz veins (formation of mode I fractures, stage 2; Fig.13b);~~

~~3. During stage 3, the mylonite and the veins were overprinted by viscous creep under increased differential stress towards what is now the BFZ045 brittle fault core (Fig.13.c);~~

~~4. During stage 4, cataclastic deformation and local generation of pseudotachylytes along the mylonitic foliation overprinted all the pre-existing structures (Fig.13.d).~~

The two models are not mutually exclusive and are both equally valid to explain our observations. We are unable to discern between the two options, due to the limiations of our P-T estimates. However, the presence of pseudotachylytes along the BFZ045 fault core indicates that the fault was capable of generating earthquakes, and the seismogenic behaviour of other faults in the Olkiluoto basement has been previously discussed (Marchesini et al., 2019 and references therein). This suggests that transient seismic loading might have triggered the localised increase in creep rate during mylonitisatoin of BFZ045.

Conclusions

This study shows that deformation microstructures can be used to evaluate the stress history of a ~~narrowing~~ shear zone deforming across the brittle-ductile transition in the continental crust, and to reconstruct the cyclical brittle-ductile deformation history of fault zones ~~that experienced cyclical brittle-ductile fault slips~~. The fault zone BFZ045 exploited a mylonitic precursor in the Paleoproterozoic basement in SW Finland, and records transient brittle deformation in the form of syn-kinematic quartz veins emplaced during ongoing mylonitic creep at ~ 450° C and 3.5 kbar, in response to transiently high fluid pressure. Mylonitic deformation continued after ~~the~~ vein emplacement, as evidenced by the dynamic recrystallization of the vein quartz. Mylonitic creep occurred under progressively increasing differential stress ~~localised~~ towards the shear zone centre in an overall narrowing shear zone ~~that was deforming under slightly decreasing T from 400-500° C to ≥ 320° C~~. Mylonitic deformation at the shear zone centre records peak stress conditions of around 120 MPa, and was followed by brittle deformation that generated cataclasites and minor pseudotachylytes in the fault core. ~~The entire deformation history documented in this study occurred at the base of the seismogenic crust at an estimated depth range of 9-13 km.~~

The constraints derived from microstructural analysis shaped the proposed conceptual model of the evolution of BFZ045 slip behaviour, which highlights the important role of transiently sub-lithostatic fluid pressure in triggering vein emplacement during ongoing mylonitic deformation, as well as of the progressive increase in stress and strain rate during viscous creep towards peak conditions reached at the BDTZ in the Fennoscandian Shield. This study shows that microstructural ~~study~~studies leading to the acquisition of independent constraints ~~offers~~offer the potential to reconstruct in detail the evolutionary history of fault zones that experienced a transition in deformation mode at the BDTZ. In addition to deriving a conceptual model of varying fault slip behaviours at the BDTZ, the methods and the results of this work complement and expand thorough site characterization studies of deep geological disposal facilities.

Acknowledgements

This study has been funded by Posiva Oy (project no. 2104442) and by the University of Plymouth. Stephen F. Cox, ~~and~~ Michael Stipp and Francesco Giuntoli are thanked for fruitful discussions in the course of the project. Glenn Harper is thanked for support during SEM and EBSD analysis at the Electron Microscopy Centre of the University of Plymouth. Andrea Risplendente is thanked for support with EMPA analysis at the University of Milan. Many thanks go to Fabrizio Nestola for giving us access to the microRaman spectrometer of the University of Padova. Danilo Bersani is thanked for support with Raman analysis at the University of Parma. Alfredo Camacho and Georg Dresen are thanked for their reviews, which helped us prepare a much improved version of the manuscript.

References

Aaltonen, I., Lahti, M., Engström, J., Mattila, J., Paananen, M., Paulamäki, S., Gehör, S., Kärki, A., Ahokas, T., Torvela, T. and Front, K.: Geological Model of the Olkiluoto Site. Version 2.0., Posiva Working Report 2010-70, Posiva Oy, Eurajoki, 2010.

Aaltonen, I., Engström, J., Gehör, S., Kosunen, P. and Kärki, A.: Geology of Olkiluoto, Posiva Working Report 2016-16, Posiva Oy, Eurajoki, 2016.

Aoya, M., Kouketsu, Y., Endo, S., Shimizu, H., Mizukami, T., Nakamura, D. and Wallis, S.: Extending the applicability of the Raman carbonaceous-material geothermometer using data from contact metamorphic rocks, Journal of Metamorphic Geology, 28(9), 895–914, doi:10.1111/j.1525-1314.2010.00896.x, 2010.

~~Austrheim, H.: Fluid and deformation induced metamorphic processes around Moho beneath continent collision zones: Examples from the exposed root zone of the Caledonian mountain belt, W-Norway, Tectonophysics, 609, 620-635, doi:10.1016/j.tecto.2013.08.030, 2013.~~

Behr, W. M. and Platt, J. P.: A naturally constrained stress profile through the middle crust in an extensional terrane, Earth and Planetary Science Letters, 303(3), 181–192, doi:10.1016/j.epsl.2010.11.044, 2011.

Bestmann, M. and Prior, D. J.: Intragranular dynamic recrystallization in naturally deformed calcite marble: diffusion accommodated grain boundary sliding as a result of subgrain rotation recrystallization, Journal of Structural Geology, 25(10), 1597–1613, doi:10.1016/S0191-8141(03)00006-3, 2003.

Beyssac, O., Goffé, B., Chopin, C. and Rouzaud, J. N.: Raman spectra of carbonaceous material in metasediments: a new geothermometer, Journal of Metamorphic Geology, 20(9), 859–871, doi:10.1046/j.1525-1314.2002.00408.x, 2002.

Bons, P. D., Elburg, M. A. and Gomez-Rivas, E.: A review of the formation of tectonic veins and their microstructures, Journal of Structural Geology, 43, 33–62, doi:10.1016/j.jsg.2012.07.005, 2012.

~~Bos, B. and Spiers, C. J.: Frictional-viscous flow of phyllosilicate-bearing fault rock: Microphysical model and implications for crustal strength profiles, Journal of Geophysical Research: Solid Earth, 107(B2), ECV 1-1-ECV 1-13, doi:10.1029/2001JB000301, 2002.~~

Ceccato, A., Menegon, L., Pennacchioni, G. and Morales, L. F. G.: Myrmekite and strain weakening in granitoid mylonites, Solid Earth, 9(6), 1399–1419, doi:https://doi.org/10.5194/se-9-1399-2018, 2018.

Cox, S. F.: Faulting processes at high fluid pressures: An example of fault valve behavior from the Wattle Gully Fault, Victoria, Australia, Journal of Geophysical Research: Solid Earth, 100(B7), 12841–12859, doi:10.1029/95JB00915, 1995.

Cox, S. F.: ~~Structural and isotopic constraints on fluid flow regimes and fluid pathways during upper crustal deformation: An example from the Taemas area of the Lachlan Orogen, SE Australia, Journal of Geophysical Research: Solid Earth, 112(B8), doi:10.1029/2006JB004734, 2007.~~

~~Cox, S. F.:~~ The application of failure mode diagrams for exploring the roles of fluid pressure and stress states in controlling styles of fracture-controlled permeability enhancement in faults and shear zones, Geofluids, doi:10.1111/j.1468-8123.2010.00281.x, 2010.

Cross, A. J., Prior, D. J., Stipp, M. and Kidder, S.: The recrystallized grain size piezometer for quartz: An EBSD-based calibration: EBSD-Based Quartz Grain Size Piezometer, Geophysical Research Letters, 44(13), 6667–6674, doi:10.1002/2017GL073836, 2017.

Derez, T., Pennock, G., Drury, M. and Sintubin, M.: Low-temperature intracrystalline deformation microstructures in quartz, Journal of Structural Geology, 71, 3–23, doi:10.1016/j.jsg.2014.07.015, 2015.

~~Dunlap, W. J., Hirth, G. and Teyssier, C.: Thermomechanical evolution of a ductile duplex, Tectonics, 16(6), 983–1000, doi:10.1029/97TC00614, 1997.~~

Eberlei, T., Habler, G., Grasemann, B. and Abart, R.: Upper–greenschist facies intragrain deformation of albite in mylonitic meta–pegmatite and the influence of crystallographic anisotropy on microstructure formation, Journal of Structural Geology, 69, 47–58, doi:10.1016/j.jsg.2014.10.001, 2014.

Fossen, H. and Cavalcante, G. C. G.: Shear zones – A review, Earth-Science Reviews, 171, 434–455, doi:10.1016/j.earscirev.2017.05.002, 2017.

Freeman, J. J., Wang, A., Kuebler, K. E., Jolliff, B. L. and Haskin, L. A.: Characterization of natural feldspars by Raman spectroscopy for future planetary exploration, The Canadian Mineralogist, 46(6), 1477–1500, 2008.

Fusseis, F. and Handy, M. R.: Micromechanisms of shear zone propagation at the brittle–viscous transition, Journal of Structural Geology, 30(10), 1242–1253, doi:10.1016/j.jsg.2008.06.005, 2008.

Giuntoli, F., Menegon, L. and Warren, C. J.: Replacement reactions and deformation by dissolution and precipitation processes in amphibolites, Journal of Metamorphic Geology, 36(9), 1263–1286, doi:10.1111/jmg.12445, 2018.

~~Gueydan, F., Leroy, Y. M., Jolivet, L. and Agard, P.: Analysis of continental midcrustal strain localization induced by microfracturing and reaction-softening, Journal of Geophysical Research: Solid Earth, 108(B2), doi:10.1029/2001JB000611, 2003.~~

~~Handy, M. R. and Brun, J.-P.: Seismicity, structure and strength of the continental lithosphere, Earth and Planetary Science Letters, 223(3), 427–441, doi:10.1016/j.epsl.2004.04.021, 2004.~~

~~Handy, M. R., Franz, L., Heller, F., Janott, B. and Zurbriggen, R.: Multistage accretion and exhumation of the continental crust (Ivrea crustal section, Italy and Switzerland), Tectonics, 18(6), 1154–1177, doi:10.1029/1999TC900034, 1999.~~

Handy, M. R., Hirth, G. and Hovius, N.: Continental Fault Structure and Rheology from the Frictional-to-Viscous Transition Downward, in Tectonic Faults: Agents of Change on a Dynamic Earth, MITP. [online] Available from: https://ieeexplore.ieee.org/document/6285583 (Accessed 13 July 2019), 2007.

Hey, M. H.: A new review of the chlorites, Mineral. Mag. J. M. Soc., 224, 277–292, https://doi.org/10.1180/minmag.1954.030.224.01, 1954.

Hentschel, F., Trepmann, C. A. and Janots, E.: Deformation of feldspar at greenschist facies conditions – the record of mylonitic pegmatites from the Pfunderer Mountains, Eastern Alps, Solid Earth, 10(1), 95–116, doi:https://doi.org/10.5194/se-10-95-2019, 2019.

Hirth, G. and Beeler, N. M.: The role of fluid pressure on frictional behavior at the base of the seismogenic zone, Geology, 43(3), 223–226, doi:10.1130/G36361.1, 2015.

Hirth, G. and Tullis, J.: Dislocation creep regimes in quartz aggregates, Journal of Structural Geology, 14(2), 145–159, doi:10.1016/0191-8141(92)90053-Y, 1992.

Hirth, G. and Tullis, J.: The brittle-plastic transition in experimentally deformed quartz aggregates, Journal of Geophysical Research: Solid Earth, 99(B6), 11731–11747, doi:10.1029/93JB02873, 1994.

Hirth, G., Teyssier, C. and Dunlap, J. W.: An evaluation of quartzite flow laws based on comparisons between experimentally and naturally deformed rocks, Int J Earth Sci, 90(1), 77–87, doi:10.1007/s005310000152, 2001.

Kärki, A. and Paulamäki, S.: Petrology of Olkiluoto, 2006.

Kidder, S., Hirth, G., Avouac, J.-P. and Behr, W.: The influence of stress history on the grain size and microstructure of experimentally deformed quartzite, Journal of Structural Geology, 83, 194–206, doi:10.1016/j.jsg.2015.12.004, 2016.

Kirilova, M., Toy, V., Rooney, J. S., Giorgetti, C., Gordon, K. C., Collettini, C. and Takeshita, T.: Structural disorder of graphite and implications for graphite thermometry., Solid Earth, 9(1), 2018.

Kjøll, H. J., Viola, G., Menegon, L. and Sørensen, B. E.: Brittle–viscous deformation of vein quartz under fluid-rich lower greenschist facies conditions, Solid Earth, 6(2), 681–699, doi:https://doi.org/10.5194/se-6-681-2015, 2015.

Kohlstedt, D. L., Evans, B. and Mackwell, S. J.: Strength of the lithosphere: Constraints imposed by laboratory experiments, Journal of Geophysical Research: Solid Earth, 100(B9), 17587–17602, doi:10.1029/95JB01460, 1995.

Kouketsu, Y., Mizukami, T., Mori, H., Endo, S., Aoya, M., Hara, H., Nakamura, D. and Wallis, S.: A new approach to develop the Raman carbonaceous material geothermometer for low-grade metamorphism using peak width, Island Arc, 23(1), 33–50, doi:10.1111/iar.12057, 2014.

~~Kukkonen, I. T. and Lauri, L. S.: Modelling the thermal evolution of a collisional Precambrian orogen: High heat production migmatitic granites of southern Finland, Precambrian Research, 168(3), 233–246, doi:10.1016/j.precamres.2008.10.004, 2009.~~

~~Küster, M. and Stöckhert, B.: High differential stress and sublithostatic pore fluid pressure in the ductile regime — microstructural evidence for short-term post-seismic creep in the Sesia Zone, Western Alps, Tectonophysics, 303(1), 263–277, doi:10.1016/S0040-1951(98)00256-X, 1999.~~

Lafuente, B., Downs, R. T., Yang, H. and Stone, N.: The power of databases: the RRUFF project, in Highlights in mineralogical crystallography, pp. 1–29, Walter de Gruyter GmbH., 2016.

Lahtinen, R.: Crustal evolution of the Svecofennian and Karelian domains during 2.1 - 1.79 Ga: with special emphasis on the geochemistry and origin of 1.93 - 1.91 Ga gneissic tonalites and associated supracrustal rocks in the Rautalampi area, central Finland ; with 7 tables, Geologian Tutkimuskeskus, Espoo., 1994.

Lahtinen, R., Korja, A. and Nironen, M.: Chapter 11 Paleoproterozoic tectonic evolution, in Developments in Precambrian Geology, vol. 14, edited by M. Lehtinen, P. A. Nurmi, and O. T. Rämö, pp. 481–531, Elsevier., 2005.

Lanari, P., Wagner, T. and Vidal, O.: A thermodynamic model for di-trioctahedral chlorite from experimental and natural data in the system MgO–FeO–Al 2 O 3–SiO 2–H 2 O: applications to P–T sections and geothermometry, Contributions to Mineralogy and Petrology, 167(2), 968, 2014.

Mänttäri, I., Talikka, M., Paulamäki, S. and Mattila, J.: U-Pb ages for tonalitic gneiss, pegmatitic granite, and diabase dyke, Olkiluoto study site, Eurajoki, SW Finland, Posiva Oy., 2006.

Mänttäri, I., Engstroem, J., Lahaye, Y. and Pere, T.: U-Pb ages for PGR dykes, KFP, and adjacent older leucosomic PGRs from ONKALO underground research facility, Olkiluoto, Eurajoki, SW Finland, Posiva Oy., 2010.

Marchesini, B., Garofalo, P. S., Menegon, L., Mattila, J. and Viola, G.: Fluid-mediated, brittle–ductile deformation at seismogenic depth – Part 1: Fluid record and deformation history of fault veins in a nuclear waste repository (Olkiluoto Island, Finland), Solid Earth, 10(3), 809–838, doi:https://doi.org/10.5194/se-10-809-2019, 2019.

Massonne, H.-J. and Schreyer, W.: Phengite geobarometry based on the limiting assemblage with K-feldspar, phlogopite, and quartz, Contributions to Mineralogy and Petrology, 96(2), 212–224, 1987.

Mattila, J. and Viola, G.: New constraints on 1.7 Gyr of brittle tectonic evolution in southwestern Finland derived from a structural study at the site of a potential nuclear waste repository (Olkiluoto Island), Journal of Structural Geology, 67, 50–74, 2014.

Melosh, B. L., Rowe, C. D., Gerbi, C., Smit, L. and Macey, P.: Seismic cycle feedbacks in a mid-crustal shear zone, Journal of Structural Geology, 112, 95–111, doi:10.1016/j.jsg.2018.04.004, 2018.

Menegon, L., Pennacchioni, G~~., Malaspina, N., Harris, K. and Wood, E.: Earthquakes as Precursors of Ductile Shear Zones in the Dry and Strong Lower Crust, Geochemistry, Geophysics, Geosystems, 18(12), 4356–4374, doi:10.1002/2017GC007189, 2017.~~. and Spiess, R.: Dissolution-precipitation creep of K-feldspar in mid-crustal granite mylonites, Journal of Structural Geology, 30(5), 565–579, doi:10.1016/j.jsg.2008.02.001, 2008.

Nguyen, P. T., Harris, L. B., Powell, C. M. and Cox, S. F.: Fault-valve behaviour in optimally oriented shear zones: an example at the Revenge gold mine, Kambalda, Western Australia, Journal of Structural Geology, 20(12), 1625–1640, doi:10.1016/S0191-8141(98)00054-6, 1998.

Nironen, M.: The Svecofennian Orogen: a tectonic model, Precambrian Research, 86(1–2), 21–44, 1997.

Nordbäck, N. and Mattila, J.: Brittle Fault Systems of the ONKALO Underground Research Facility, 2018.

Pajunen, M., Airo, M., Elminen, T., Mänttäri, I., Niemelä, R., Vaarma, M., Wasenius, P. and Wennerström, M.: Tectonic evolution of the Svecofennian crust in southern Finland, Geological Survey of Finland, Special Paper, 47, 15–160, 2008.

Pennacchioni, G. and Mancktelow, N. S.: Nucleation and initial growth of a shear zone network within compositionally and structurally heterogeneous granitoids under amphibolite facies conditions, Journal of Structural Geology, 29(11), 1757–1780, doi:10.1016/j.jsg.2007.06.002, 2007.

Pere, T.: Fault-related local phenomena in the bedrock of Olkiluoto with particular reference to fault zone OL-BFZ100, Posiva Oy., 2009.

~~Pfiffner, O. A.: Basement-involved thin-skinned and thick-skinned tectonics in the Alps, Geological Magazine, 153(5–6), 1085–1109, doi:10.1017/S0016756815001090, 2016.~~

~~Pitzer, K. S. and Sterner, S. M.: Equations of state valid continuously from zero to extreme pressures for H2O and CO2, J. Chem. Phys., 101(4), 3111–3116, doi:10.1063/1.467624, 1994.~~

~~Ranalli, G.: Rheology of the lithosphere in space and time, Geological Society, London, Special Publications, 121(1), 19–37, doi:10.1144/GSL.SP.1997.121.01.02, 1997.~~

Saintot, A., Stephens, M., Viola, G. and Nordgulen, Ø.: Brittle tectonic evolution and paleostress field reconstruction in the southwestern part of the Fennoscandian Shield, Forsmark, Sweden, Tectonics, 30(4), 2011.

~~Scholz, C.: The Mechanics of Earthquakes and Faulting, Cambridge University Press, Cambridge., 1990.~~

Scholz, C. H.: Earthquakes and friction laws, Nature, 391(6662), 37, doi:10.1038/34097, 1998.

~~Sibson, R. H.: Fault zone models, heat flow, and the depth distribution of earthquakes in the continental crust of the United States, Bulletin of the Seismological Society of America, 72(1), 151–163, 1982.~~

~~Sibson, R. H.: A note on fault reactivation, Journal of Structural Geology, 7(6), 751–754, doi:10.1016/0191-8141(85)90150-6, 1985.~~

Sibson, R. H.: Earthquake faulting as a structural process, Journal of Structural Geology, 11(1), 1–14, doi:10.1016/0191-8141(89)90032-1, 1989.

Sibson, R. H.: Conditions for fault-valve behaviour, Geological Society, London, Special Publications, 54(1), 15–28, doi:10.1144/GSL.SP.1990.054.01.02, 1990.

Sibson, R. H.: Implications of fault-valve behaviour for rupture nucleation and recurrence, Tectonophysics, 211(1), 283–293, doi:10.1016/0040-1951(92)90065-E, 1992.

Sibson, R. H.: Load-strengthening versus load-weakening faulting, Journal of Structural Geology, 15(2), 123–128, doi:10.1016/0191-8141(93)90090-W, 1993.

Sibson, R. H. and Rowland, J. V.: Stress, fluid pressure and structural permeability in seismogenic crust, North Island, New Zealand, Geophys J Int, 154(2), 584–594, doi:10.1046/j.1365-246X.2003.01965.x, 2003.

Skyttä, P. and Torvela, T.: Brittle reactivation of ductile precursor structures: The role of incomplete structural transposition at a nuclear waste disposal site, Olkiluoto, Finland, Journal of Structural Geology, 116, 253–259, 2018.

Stipp, M. and Kunze, K.: Dynamic recrystallization near the brittle-plastic transition in naturally and experimentally deformed quartz aggregates, Tectonophysics, 448(1), 77–97, doi:10.1016/j.tecto.2007.11.041, 2008.

Stipp, M. and Tullis, J.: The recrystallized grain size piezometer for quartz, Geophysical Research Letters, 30(21), doi:10.1029/2003GL018444, 2003.

Stipp, M., Stünitz, H., Heilbronner, R. and Schmid, S. M.: The eastern Tonale fault zone: a 'natural laboratory' for crystal plastic deformation of quartz over a temperature range from 250 to 700°C, Journal of Structural Geology, 24(12), 1861–1884, doi:10.1016/S0191-8141(02)00035-4, 2002.

Stipp, M., Tullis, J., Scherwath, M. and Behrmann, J. H.: A new perspective on paleopiezometry: Dynamically recrystallized grain size distributions indicate mechanism changes, Geology, 38(8), 759–762, doi:10.1130/G31162.1, 2010.

Stöckhert, B., Brix, M. R., Kleinschrodt, R., Hurford, A. J. and Wirth, R.: Thermochronometry and microstructures of quartz—a comparison with experimental flow laws and predictions on the temperature of the brittle–plastic transition, Journal of Structural Geology, 21(3), 351–369, doi:10.1016/S0191-8141(98)00114-X, 1999.

~~Streit, J. E. and Cox, S. F.: Fluid pressures at hypocenters of moderate to large earthquakes, Journal of Geophysical Research: Solid Earth, 106(B2), 2235–2243, doi:10.1029/2000JB900359, 2001.~~

Stünitz, H. and Gerald, J. D. F.: Deformation of granitoids at low metamorphic grade. II: Granular flow in albite-rich mylonites, Tectonophysics, 221(3), 299–324, doi:10.1016/0040-1951(93)90164-F, 1993.

Stünitz, H., Fitz Gerald, J. D. and Tullis, J.: Dislocation generation, slip systems, and dynamic recrystallization in experimentally deformed plagioclase single crystals, Tectonophysics, 372(3), 215–233, doi:10.1016/S0040-1951(03)00241-5, 2003.

~~Suominen, V.: The chronostratigraphy of southwestern Finland with special reference to Postjotnian and Subjotnian diabases, Espoo., 1991.~~

Torgersen, E., Viola, G., Zwingmann, H. and Harris, C.: Structural and temporal evolution of a reactivated brittle–ductile fault – Part II: Timing of fault initiation and reactivation by K–Ar dating of synkinematic illite/muscovite, Earth and Planetary Science Letters, 410, 212–224, doi:10.1016/j.epsl.2014.09.051, 2015.

Torvela, T. and Ehlers, C.: From ductile to brittle deformation: structural development and strain distribution along a crustal-scale shear zone in SW Finland, International Journal of Earth Sciences, 99(5), 1133–1152, 2010.

Trepmann, C. A. and Seybold, L.: Deformation at low and high stress-loading rates, Geoscience Frontiers, 10(1), 43–54, doi:10.1016/j.gsf.2018.05.002, 2019.

~~Trepmann, C. A. and Stöckhert, B.: Quartz microstructures developed during non-steady state plastic flow at rapidly decaying stress and strain rate, Journal of Structural Geology, 25(12), 2035–2051, doi:10.1016/S0191-8141(03)00073-7, 2003.~~

~~Trepmann, C. A. and Stöckhert, B.: Short-wavelength undulatory extinction in quartz recording coseismic deformation in the middle crust – an experimental study, Solid Earth, 4(2), 263–276, doi:https://doi.org/10.5194/se-4-263-2013, 2013.~~

Trepmann, C. A., Stöckhert, B., Dorner, D., Moghadam, R. H., Küster, M. and Röller, K.: Simulating coseismic deformation of quartz in the middle crust and fabric evolution during postseismic stress relaxation — An experimental study, Tectonophysics, 442(1), 83–104, doi:10.1016/j.tecto.2007.05.005, 2007.

~~Trepmann, C. A., Hsu, C., Hentschel, F., Döhler, K., Schneider, C. and Wichmann, V.: Recrystallization of quartz after low-temperature plasticity – The record of stress relaxation below the seismogenic zone, Journal of Structural Geology, 95, 77–92, doi:10.1016/j.jsg.2016.12.004, 2017~~.

Tuisku, P. and Kärki, A.: Metamorphic petrology of Olkiluoto, Posiva Oy., 2010.

Viola, G., Mancktelow, N. S. and Miller, J. A.: Cyclic frictional-viscous slip oscillations along the base of an advancing nappe complex: Insights into brittle-ductile nappe emplacement mechanisms from the Naukluft Nappe Complex, central Namibia, Tectonics, 25(3), doi:10.1029/2005TC001939, 2006.

Viola, G., Venvik Ganerød, G. and Wahlgren, C.-H.: Unraveling 1.5 Ga of brittle deformation history in the Laxemar-Simpevarp area, southeast Sweden: A contribution to the Swedish site investigation study for the disposal of highly radioactive nuclear waste, Tectonics, 28(5), doi:10.1029/2009TC002461, 2009.

Wehrens, P., Berger, A., Peters, M., Spillmann, T. and Herwegh, M.: Deformation at the frictional-viscous transition: Evidence for cycles of fluid-assisted embrittlement and ductile deformation in the granitoid crust, Tectonophysics, 693, 66–84, doi:10.1016/j.tecto.2016.10.022, 2016.

~~White, J. C.: Transient discontinuities revisited: pseudotachylyte, plastic instability and the influence of low pore fluid pressure on deformation processes in the mid-crust, Journal of Structural Geology, 18(12), 1471–1486, doi:10.1016/S0191-8141(96)00059-4, 1996.~~

~~White, J. C.: Paradoxical pseudotachylyte – Fault melt outside the seismogenic zone, Journal of Structural Geology, 38, 11–20, doi:10.1016/j.jsg.2011.11.016, 2012.~~

Wright, S. I., Nowell, M. M. and Field, D. P.: A Review of Strain Analysis Using Electron Backscatter Diffraction, Microscopy and Microanalysis, 17(3), 316–329, doi:10.1017/S1431927611000055, 2011.

Yardley, B. and Baumgartner, L.: Fluid processes in deep crustal fault zones, Tectonic Faults–Agents of Change on a Dynamic Earth, 295–318, 2007.

Sample name	PH28_7a	PH28_7b-1	PH28_5a	PH28_5b-1	PH28_5c	PH28_5d	PH28_9e	PH28_10-6
N. measurament	n=5	n=5	n=15	n=18	n=12	n=16	n=18	n=10
Chemical composition (wt%)								
SiO2	48.280	48.080	48.210	48.410	48.330	48.770	47.970	47.660
TiO2	0.093	0.098	0.124	0.099	0.104	0.074	0.043	0.136
Al2O3	33.910	33.900	33.860	34.520	34.590	34.680	35.690	34.910
Cr2O3	0.011	0.000	0.000	0.017	0.000	0.000	0.037	0.000
Fe2O3	0.000	0.000	0.000	0.000	0.000	0.000	0.000	
FeO	2.540	2.430	2.710	2.080	2.060	1.940	3.010	2.730
MnO	0.060	0.001	0.052	0.000	0.000	0.005	0.078	0.028
MgO	1.563	1.383	1.446	1.411	1.384	1.360	0.546	1.415
CaO	0.017	0.005	0.000	0.032	0.010	0.033	0.015	0.054
Na2O	0.091	0.136	0.132	0.163	0.138	0.116	0.126	0.201
K2O	11.080	11.120	11.090	11.180	11.030	11.230	9.430	10.690
NiO	0.000	0.036	0.006	0.000	0.000	0.013	0.000	0.036
Total	97.645	97.189	97.630	97.912	97.646	98.221	96.944	97.859
Structural formula on the basis of 11 O								
SiO2	3.15	3.16	3.15	3.15	3.15	3.16	3.13	3.11
TiO2	0.00	0.00	0.01	0.00	0.01	0.00	0.00	0.01
Al2O3	2.61	2.62	2.61	2.65	2.65	2.65	2.74	2.68
Cr2O3	0.00	0.00	0.00	0.00	0.00	0.00	0.00	0.00
Fe2O3	0.00	0.00	0.00	0.00	0.00	0.00	0.00	0.00
FeO	0.14	0.13	0.15	0.11	0.11	0.11	0.16	0.15
MnO	0.00	0.00	0.00	0.00	0.00	0.00	0.00	0.00
MgO	0.15	0.14	0.14	0.14	0.13	0.13	0.05	0.14
CaO	0.00	0.00	0.00	0.00	0.00	0.00	0.00	0.00
Na2O	0.01	0.02	0.02	0.02	0.02	0.01	0.02	0.03
K2O	0.92	0.93	0.93	0.93	0.92	0.93	0.78	0.89
NiO	0.00	0.00	0.00	0.00	0.00	0.00	0.00	0.00
H2O	0.00	0.00	0.00	0.00	0.00	0.00	0.00	0.00

Table 1. Representative compositions of muscovite from the BFZ045 mylonite

Fault rock	Mylonite				Cataclasite				Veins			
Sample name	PH16-2_2	PH16-2_5	PH28-10_3	PH28-10_15	PH28-9_5	PH28-9_7	PH28-9_10	PH28-9_19	PH28-6_6	PH28-6_9	PH28-6_11	PH28-6_13
Chemical composition (wt%)												
SiO2	25.040	25.820	24.790	24.790	23.600	23.800	23.290	24.170	25.470	23.930	23.290	24.070
TiO2	0.034	0.034	0.078	0.060	0.031	0.115	0.050	0.010	0.059	0.049	0.004	0.000
Al2O3	21.600	22.290	21.890	22.140	22.150	22.420	22.440	21.990	20.620	21.860	22.690	22.120
FeO	28.700	29.930	35.830	34.600	38.530	39.650	39.150	34.360	37.260	37.940	39.670	37.650
MnO	0.173	0.349	0.918	0.858	0.846	0.810	0.793	0.675	1.201	0.596	0.937	1.430
MgO	12.010	11.740	7.570	8.430	4.810	3.780	3.900	7.730	6.980	5.810	3.910	5.730
CaO	0.047	0.061	0.121	0.056	0.008	0.001	0.003	0.000	0.021	0.006	0.005	0.044
Na2O	0.014	0.055	0.010	0.000	0.000	0.046	0.036	0.011	0.000	0.000	0.015	0.000
K2O	0.064	0.047	0.020	0.040	0.021	0.000	0.080	0.087	0.008	0.000	0.005	0.008
Total	87.682	90.364	91.236	90.973	90.049	90.655	89.742	89.033	91.620	90.190	90.525	91.081
Structural formulae on the basis of 14 O												
Si	2.687	2.695	2.658	2.647	2.610	2.624	2.595	2.641	2.741	2.628	2.577	2.621
Ti	0.003	0.003	0.006	0.005	0.003	0.010	0.004	0.001	0.005	0.004	0.000	0.000
Al	2.731	2.742	2.766	2.786	2.887	2.913	2.947	2.832	2.615	2.829	2.959	2.839
Fe(3+)	0.000	0.000	0.000	0.000	0.000	0.000	0.000	0.000	0.000	0.000	0.000	0.000
Fe(2+)	2.575	2.613	3.213	3.089	3.563	3.656	3.648	3.140	3.353	3.485	3.671	3.429
Mn	0.016	0.031	0.083	0.078	0.079	0.076	0.075	0.063	0.110	0.055	0.088	0.132
Mg	1.921	1.827	1.210	1.342	0.793	0.621	0.648	1.259	1.120	0.951	0.645	0.930
Ca	0.005	0.007	0.014	0.006	0.001	0.000	0.000	0.000	0.003	0.001	0.001	0.005
Na	0.003	0.011	0.002	0.000	0.000	0.010	0.008	0.002	0.000	0.000	0.003	0.000
K	0.009	0.006	0.003	0.005	0.003	0.000	0.011	0.012	0.001	0.000	0.001	0.001
XFe= Fe/(Fe+Mg)	0.57	0.59	0.73	0.70	0.82	0.85	0.85	0.71	0.75	0.79	0.85	0.79

Table 2. Representative compositions of chlorite from different domains of BFZ045.

Parameter	Value	Reference/source	Notes
vertical stress σ2	350 MPa	P estimate	lithostatic load during deformation for Andersonian type fault in a strike-slip regime
strain rate	stage 1 (50MPa) 4.3×10^{-13} s^{-1} stage 3 (80MPa) 1.1×10^{-12} s^{-1} stage 3 (120 MPa) 6.9×10^{-12} s^{-1}	Hirth et al. (2001) Wither's fugacity calculator (Pitzer and Sterner, 1994)	$\dot{\varepsilon} = A\sigma^n f_{H2O}^m \exp(-Q/RT)$ A an empirical constant, σ the differential stress, n the stress exponent, f_{H2O} the water fugacity (calculated at 350 MPa using Wither's fugacity calculator), m the water fugacity exponent, Q the activation energy, R the gas constant, and T the temperature
fluid pressure conditions	> 210 MPa	Marchesini et al. (2019)	
friction coefficient (μ)	0.6	Sibson (1985)	common value for granitoids
cohesive strength	26 MPa	Aaltonen et al.(2010)	data from tensile strength measurements of granitic gneisses
tensile strength	13 MPa	Aaltonen et al.(2010)	

Table 3. Parameters used for λ -σ failure mode diagrams

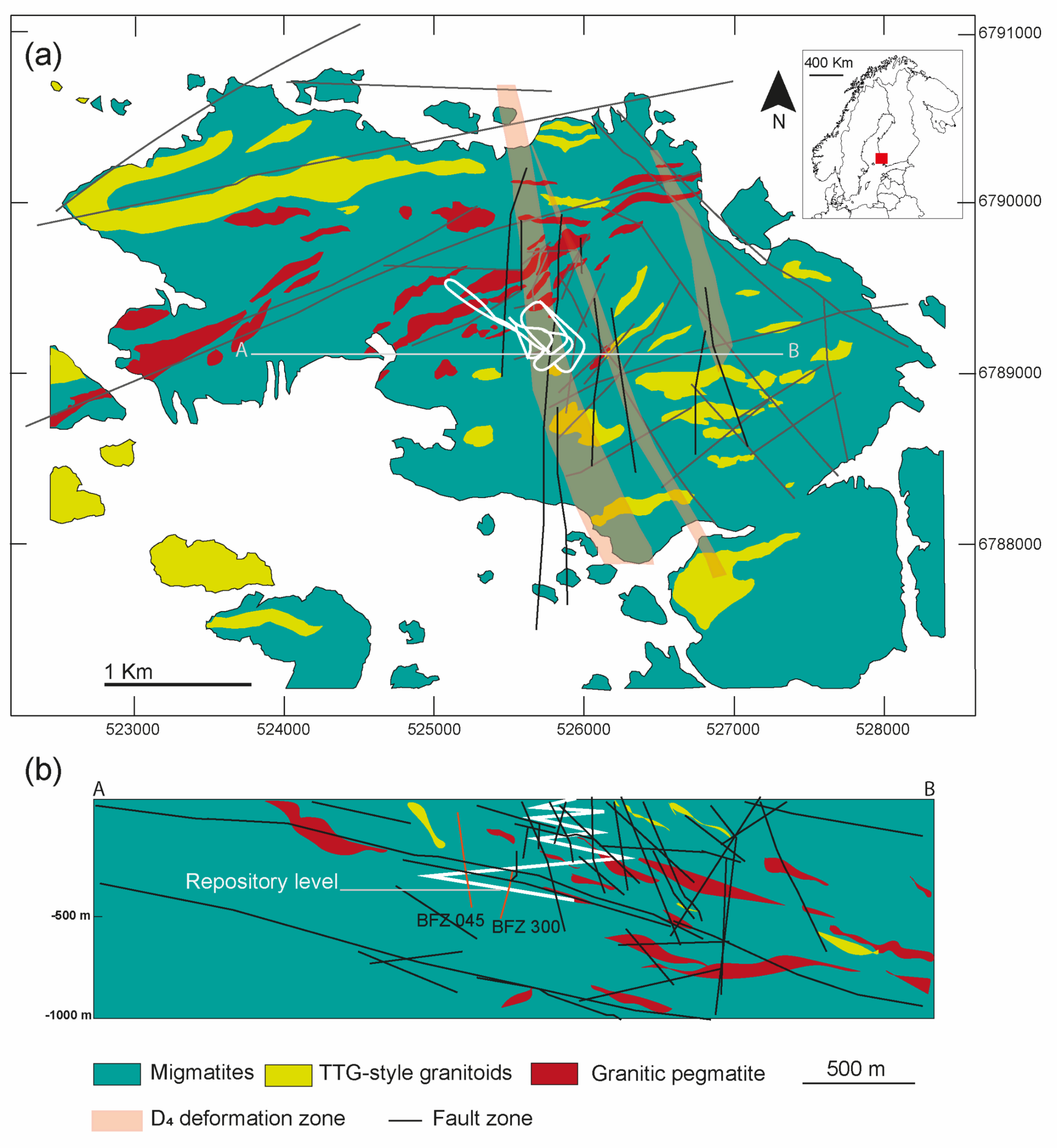

(a)
6791000
6790000
6789000
6788000
523000
524000
525000
526000
527000
528000
400 Km
N
A
B
1 Km
(b)
A
B
Repository level
BFZ 045
BFZ 300
-500 m
-1000 m
Migmatites
TTG-style granitoids
Granitic pegmatite
500 m
D₄ deformation zone
Fault zone

Figure 1. Geological setting of Olkiluoto, SW Finland (inset on top-right). (a) Schematic geological and structural map, showing surface intersection of modelled brittle fault zone (BFZ) and ductile deformation zone, modified from Aaltonen et al. (2016) and Skytta and Torvela (2018). Coordinates for zone 34N in UTM coordinate system. The white line indicates the location of the underground Onkalo facility.~~-~~ A-B is the trace of the cross section shown in (b). (b) East-west cross section across the underground infrastructure, with the tunnel shown as white line. Sub vertical fault BFZ045 described in this study and its conjugate BFZ300 are shown as orange lines.

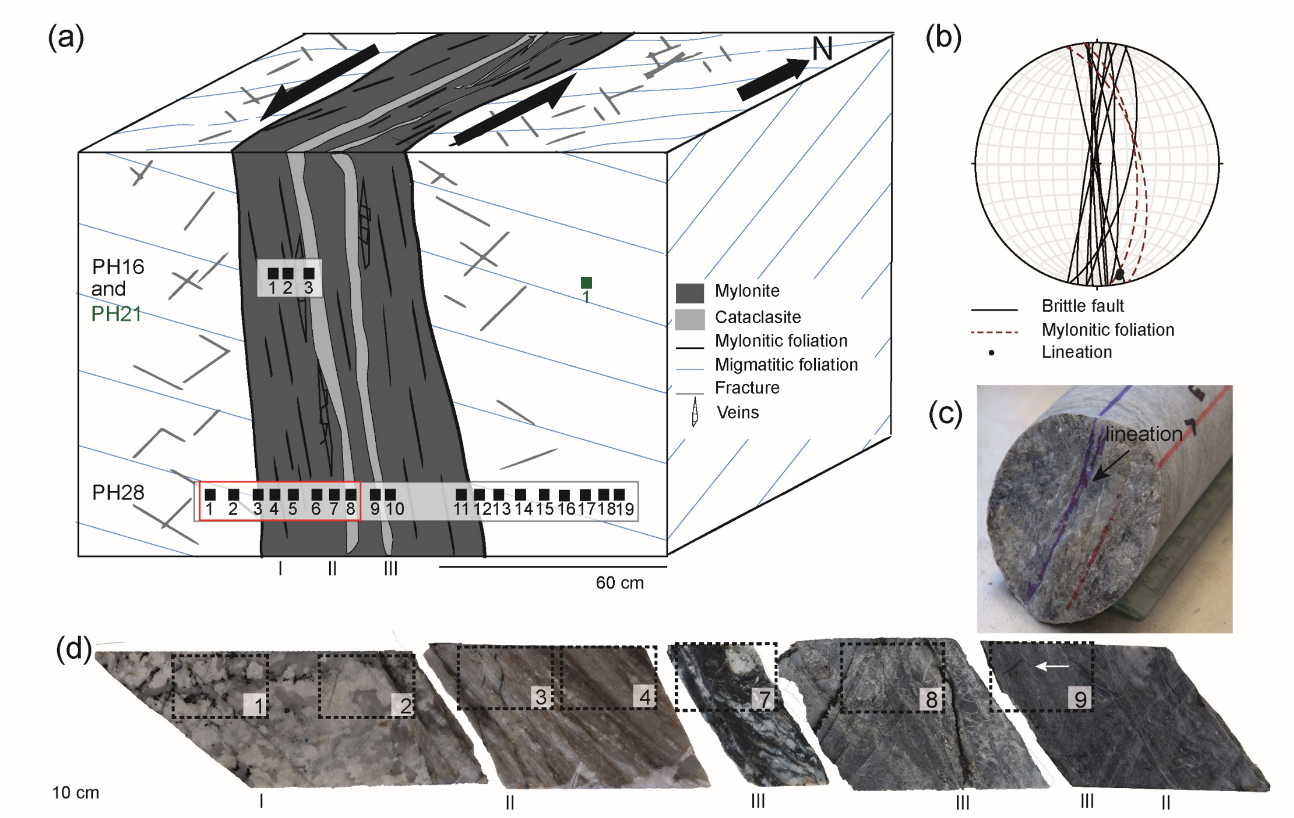

Figure 2. BFZ045 fault geometry. (a) Schematic representation of fault architecture from core logs, vertical axis not to scale. Grey rectangles locate the studied drill cores PH28 and PH16, black squares show sample location. The red rectangle indicates the samples shown in (d). (b) Stereoplot of BFZ045 fault core orientation and mylonitic foliation observed at different drill hole intersection ~~along~~in the Onkalo facility (Aaltonen et al., 2016). (c) Core sample along PH28 drill core within the fault core unit. The core sample exposes the mylonitic foliation, where the blue line indicates the stretching lineation, which is parallel to chlorite striae. ~~The red line indicates the lower part of the core~~ (d) Samples from PH28 drill core representative of different domains of the fault~~ units~~: damaged coarse-grained host rock (I), and fault core with mylonites and chlorite rich cataclasites (II-III). ~~-~~Dashed lines outline the area of petrographic thin sections. White arrow points to pseutotachylyte injection veins.

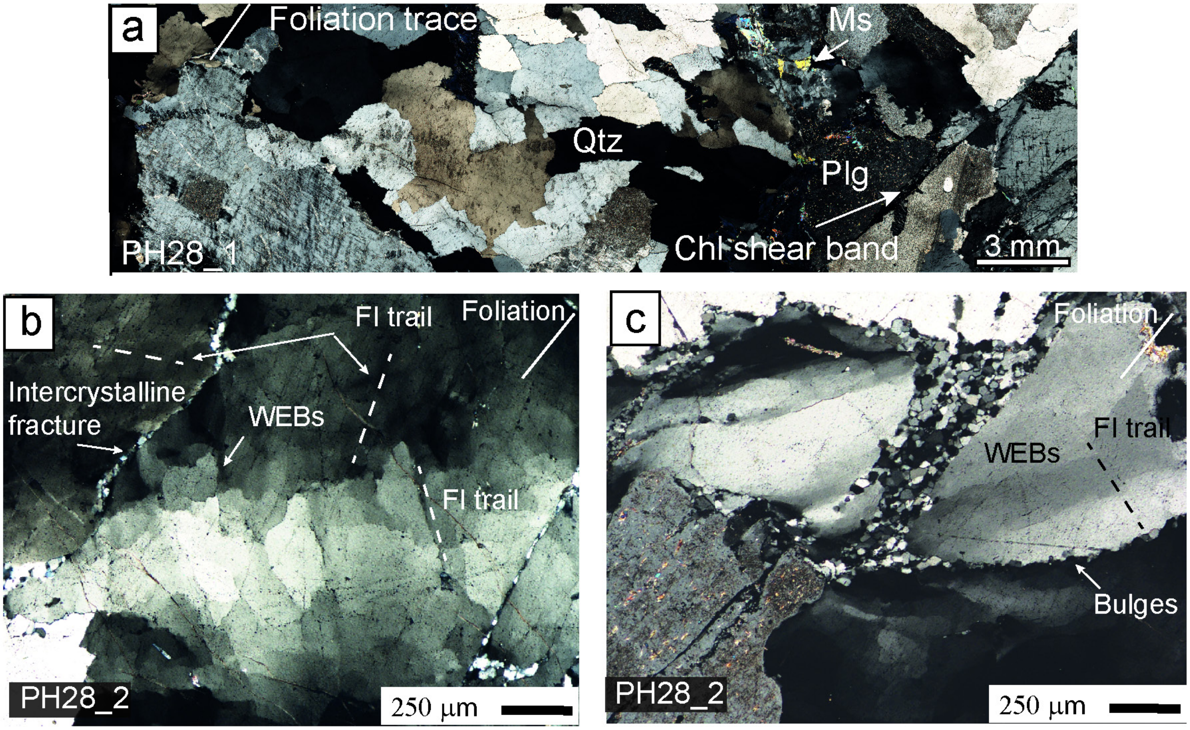

Figure 3. **Polarized light microscope images of ~~characteristic lithologies for~~ the ~~damage zone~~damaged host rock (a~~)~~), and ~~fault core~~representative quartz microstructures (b-c). ~~Stitched microphotographs in cross~~ Cross polarized light ~~and plane polarized light.~~. (a) ~~Damage zone shows~~Host rock showing the original magmatic textures and mineral assemblage ~~of the host rock~~. White arrow shows a chlorite-rich shear band oriented at a low angle to the mylonitic foliation of ~~the fault core. (b) Mylonite in the fault core. Foliation is defined by the alternation of quartz-rich and mica-rich domains. Porphyroclasts of feldspars are preferentially located in mica-rich domains. (c) Fault core cataclasite~~BFZ045. (b ~~with characteristic pseudotachylyte injection veins (arrow). The cataclasite matrix is enriched in chlorite and Ti-oxides. (d) Scanning electron microscope (SEM) image of the pseudotachylyte injection vein. Rounded quartz clast (dark grey) and Ti-oxides (white) are surrounded by a chlorite and mica rich ultrafine grained matrix.Quartz microstructures in the damage zone. Cross polarized light. (a~~) Quartz with wide extinction bands (WEBs) and undulatory extinction. WEBs are bounded by sets of fluid inclusions trails (FI trail, dashed lines). Intercrystalline deformation bands and well-developed FI trails developed sub-parallel to the mylonitic foliation. (~~b~~c) Polygonal recrystallized quartz grains, with small grain size (~20 µm), forming bands oriented sub-parallel to the mylonitic foliation. The white arrow shows sutured grain boundaries between magmatic quartz grains, indicative of bulging. Foliation trace is projected as a white line on to the images from the adjacent foliated host rock.**

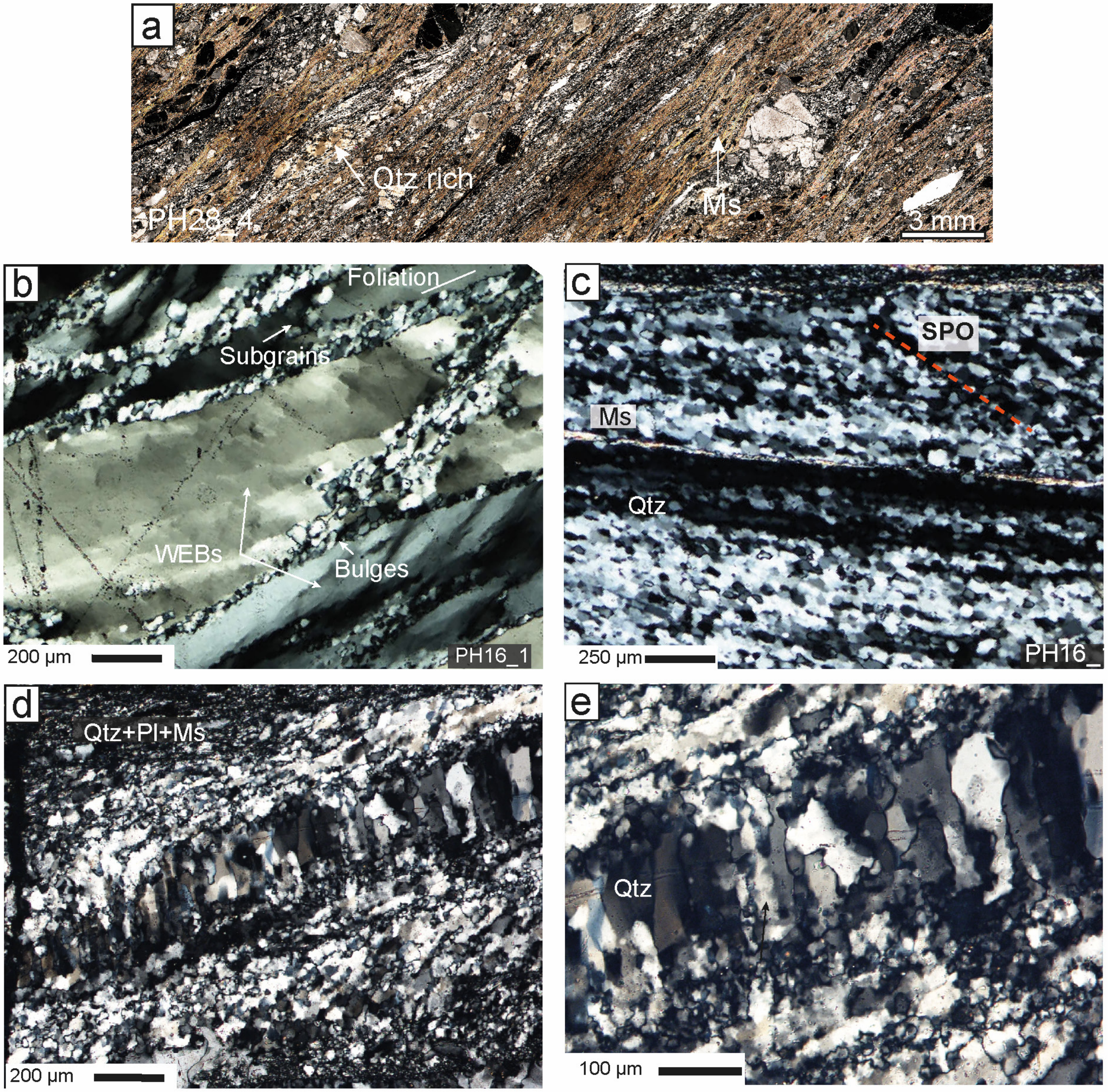

Figure 4. Microstructure of the BFZ045 mylonite. Cross-polarized light. (a) The mylonitic foliation is defined by the alternation of quartz-rich and mica-rich bands. Fractured porphyroclasts of feldspars are preferentially located in mica-rich domains. (b) ~~Figure 5. Quartz microstructures in the fault core. Microphotograph in cross polarized light. (a)~~Quartz ribbons in the shear zone boundary are stretched along the foliation and show typical core-and-mantle microstructure, with recrystallization localized at the grain boundaries. Ribbons contain also well-developed WEBs. (~~b~~c) Completely recrystallized quartz ribbon. The recrystallized grains show a shape preferred orientation indicating a sinistral sense of shear. Thin muscovite (Ms) layers define the mylonitic foliation, together with the elongated and recrystallized quartz domains. (~~c~~d) Quartz veins along the foliation, ~~infilling of~~filling a mode I fracture at a distance of ~ 1cm from the cataclasite fault core. Quartz grains elongation in the veins is normal to the vein wall and to the foliation. (~~d~~e) High magnification view of the quartz ~~infilling the~~ vein. Bulges along the grain boundaries, and subgrains within the grains are visible.

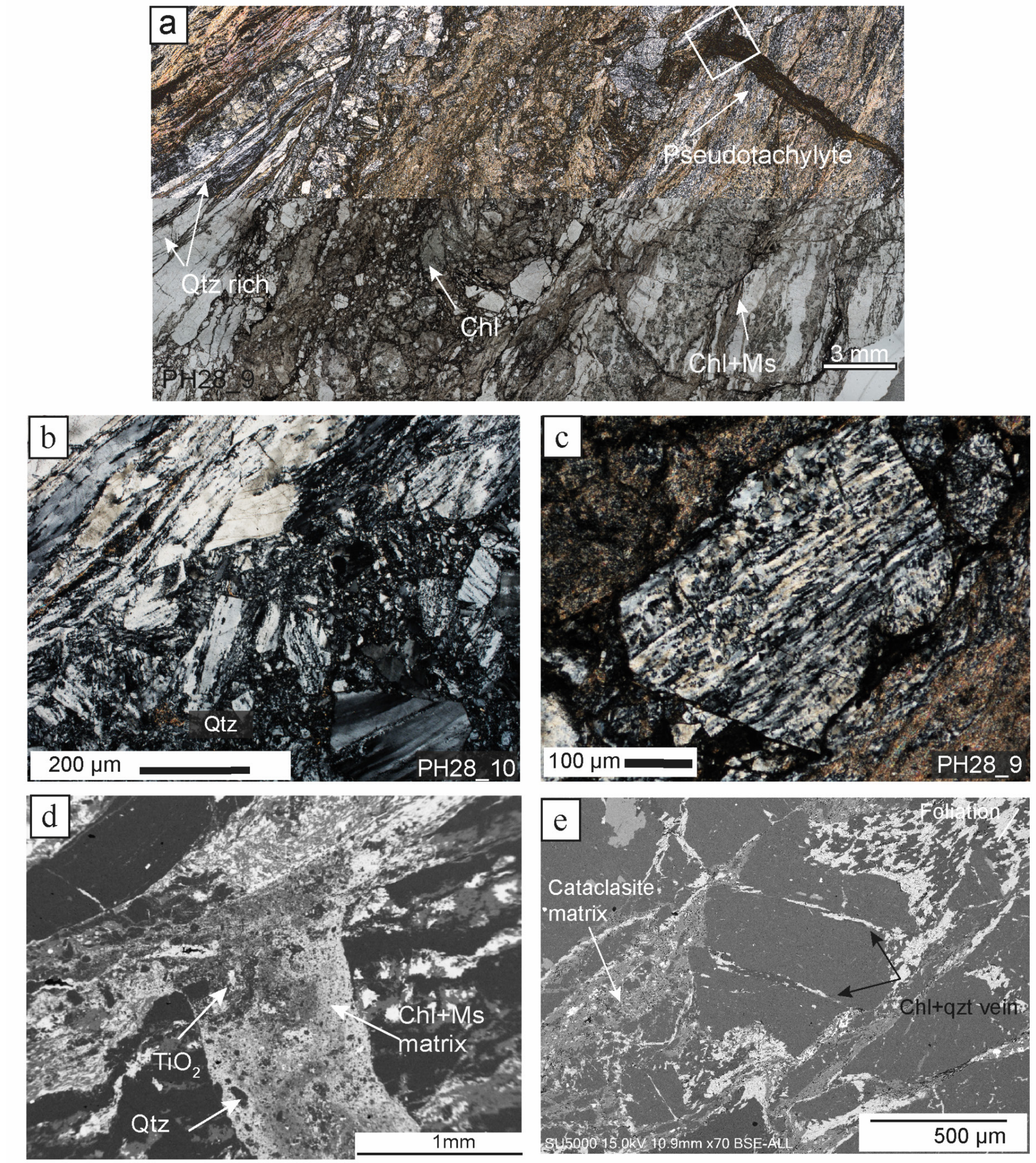

Figure 5. . Microstructure of the BFZ045 brittle fault core. Cross-polarized light (a-c), plane-polarized light (a), and scanning electron microscope backscatter electron images (SEM-BSE) (d-e). (a) Cataclasite with characteristic pseudotachylyte injection veins (arrow). The cataclasite matrix is enriched in chlorite and Ti-oxides. (~~(e~~b) Contact between the mylonite (upper left corner) and the cataclasite. Quartz ~~form~~forms almost entirely recrystallized polycrystalline ribbons. (~~f~~c) Detail of a sub-angular polycrystalline clast of quartz in the cataclasite. The trace of the mylonitic foliation is still visible in the clast, and is only slightly rotated with respect to

the trace of the foliation in the mylonite. ~~The surrounding matrix is a fine mixture of white mica and plagioclase.~~The surrounding matrix is a fine mixture of white mica and plagioclase. (d) Pseudotachylyte injection vein. Rounded quartz clast (dark grey) and Ti-oxides (white) are surrounded by a chlorite and mica rich ultrafine-grained matrix. (e) Quartz + chlorite aggregates filling fractures within and strain shadows around plagioclase porphyroclast in the mylonite. The clast is slightly rotated within the protocataclasite. The white line in the top right corner indicates the trace of the mylonitic foliation.

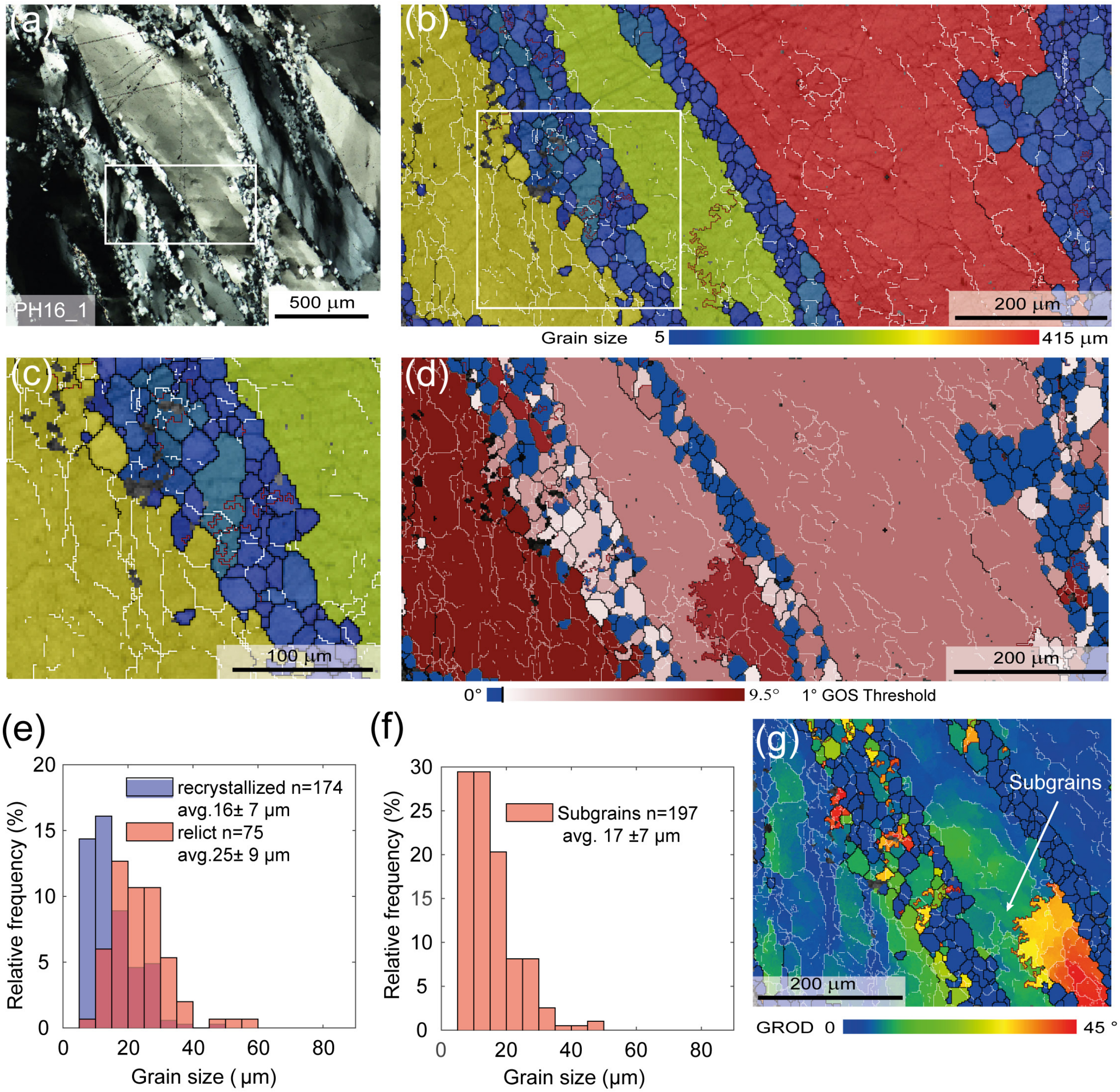

Figure 6. EBSD data of quartz from the mylonitic fault core. In all the EBSD maps, black lines correspond to high-angle boundaries (misorientation > 10°), white lines to low-angle boundaries (misorientation between 2° and 10°), and red lines to Dauphiné twin boundaries (misorientation of 60° around the c-axis). (a) Quartz ribbons and intracrystalline bands of recrystallized grains (Fig. 5a). Cross polarized light. The box locates the EBSD map shown in (b-d, g). (b-c) Grain size map (diameter of the equivalent circle, µm), the higher magnification in (c) highlights the presence of subgrains in the large relict quartz grains and in the recrystallized grains.

(d) Grain orientation spread (GOS) for each grain, coloured relative to the GOS threshold (black line) between recrystallized (blue) and relict (red) grains. (e) Histogram of grains size distribution of grains in the intercrystalline bands. (f) Histogram of subgrains size distribution of subgrains in the relict quartz from the intercrystalline bands (light red in (d)). (g) Grain Orientation Distribution maps (GROD) was used to estimate visually the subgrains size in the quartz ribbon.

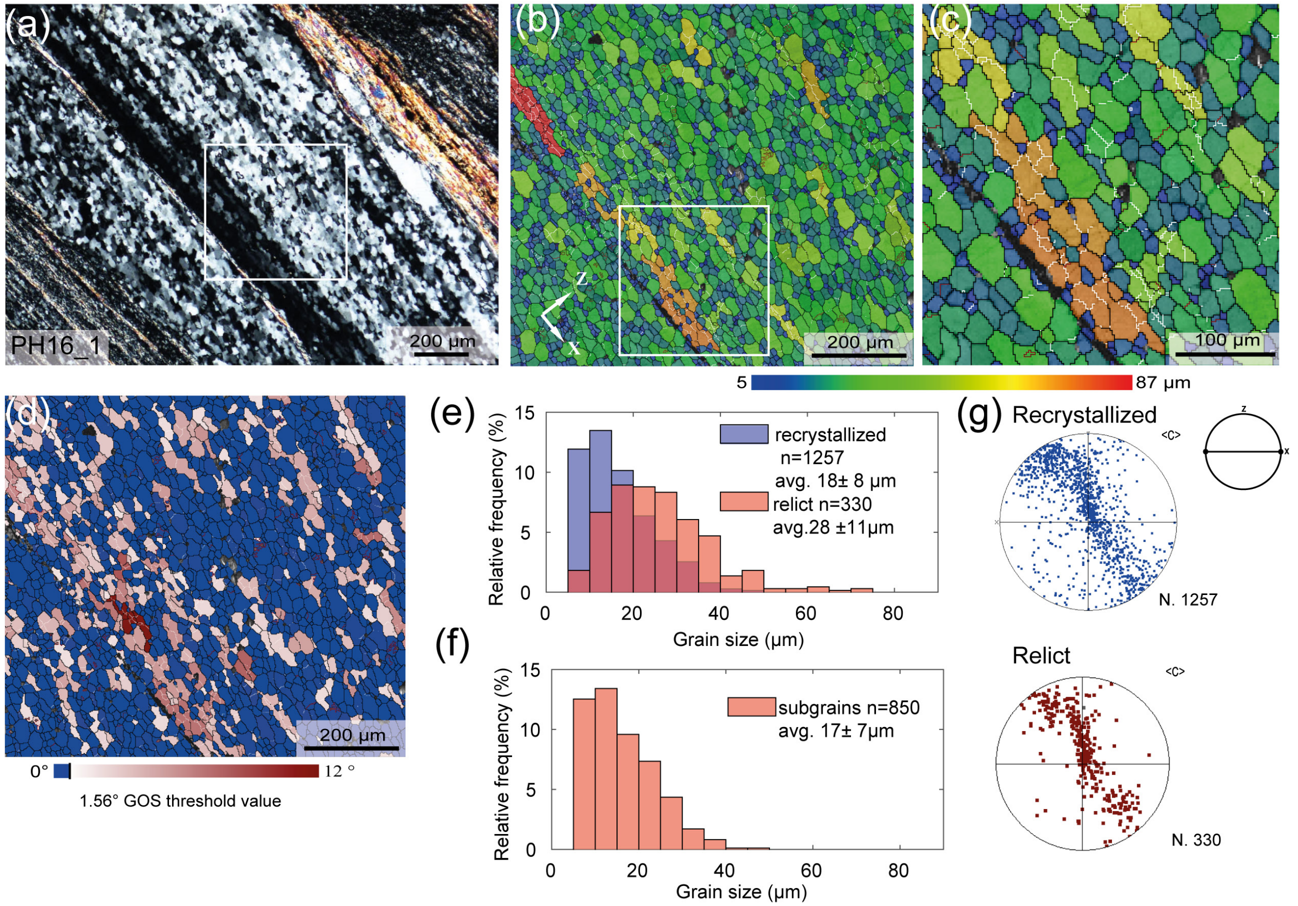

Figure 7. EBSD data of quartz from a recrystallized ribbon in the mylonite. (a) Polycrystalline ribbons of recrystallized quartz grains elongated parallel to the mylonitic foliation (Fig. 5b). Cross polarized light. The box indicates the EBSD maps shown in (b-d). Colour coding of the boundaries like in Figure 6. (b, c) Grain size map (diameter of the equivalent circle, µm) and detail (c) showing that the larger grains contain subgrains of the same size as the surrounding finer grains.(d) GOS map showing that the GOS values are mostly under the threshold, indicative of high degree of recrystallization. (e) Histogram of the grain size distribution for recrystallized and relict grains. (f) Histogram of the subgrain size distribution in the relict quartz grains identified in (d) and (e).(g) Pole figure of the c-axis orientation of recrystallized and relict grains, colour coded like the GOS map in (d). Equal area, lower hemisphere projection.

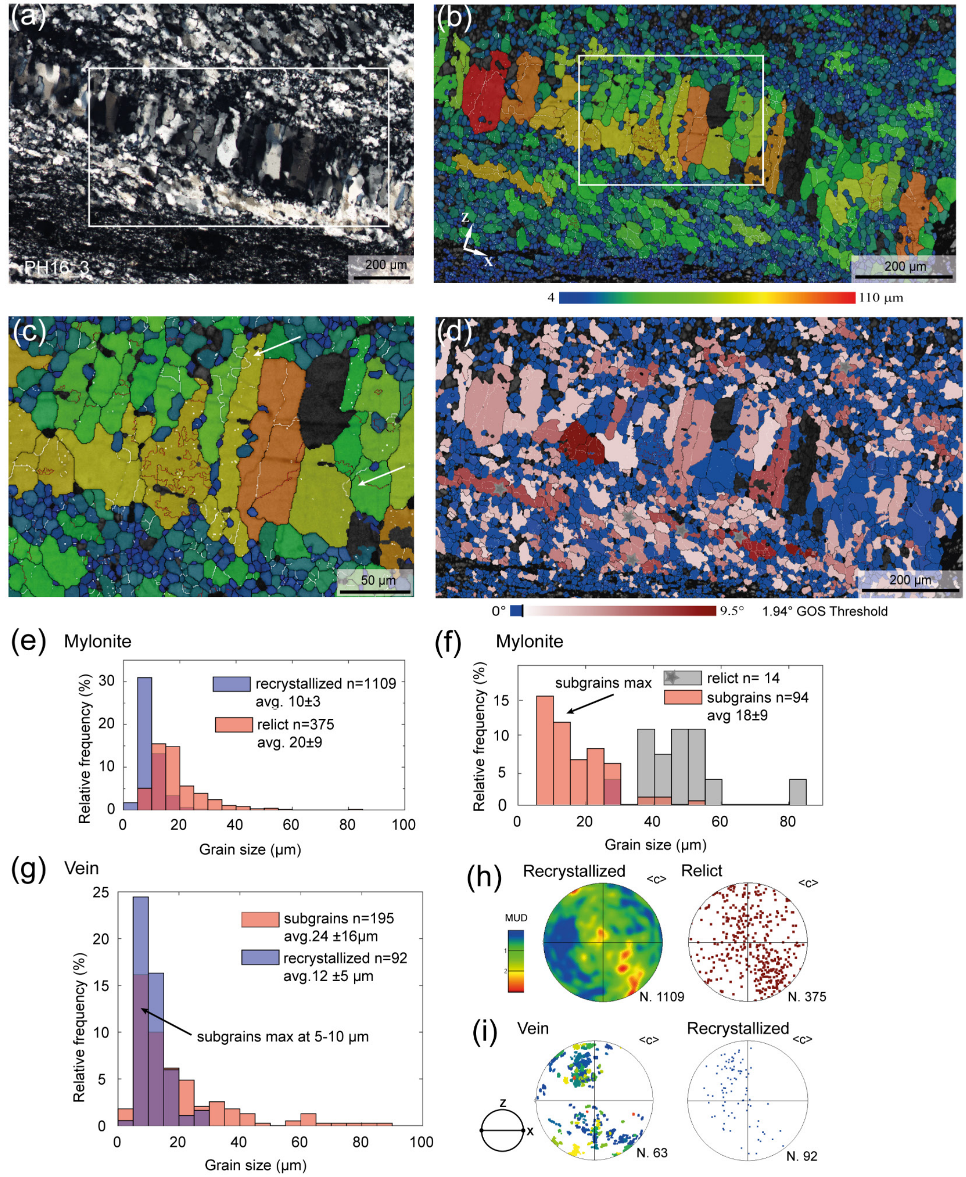

Figure 8. EBSD data of quartz from a foliation-parallel vein in the mylonite near the contact to the cataclasite. Colour coding of the boundaries like in Figure 6. (a) Quartz vein along the foliation. Quartz in the mylonite show a strong SPO consistent with the sinistral sense of shear of BFZ045. Cross polarized light. (b) Grain size map (diameter of the equivalent circle, µm. (c) Details of previous maps. Bulges and subgrains (white arrows) of similar size of the bulges are evident within the vein quartz. (d) GOS map of quartz in the vein and of the surrounding mylonite. The GOS threshold value of 1.94° separates relict grains (red) from recrystallized grains (blue).Grey stars indicate relict grains plotted in (f) for subgrain size estimates. (e) Histogram of the grain size distribution in the mylonite, with relict and recrystallized grains separated with the GOS method. (f) Histogram of the subgrain size distribution (red) in relict quartz of the mylonite (grey). (g) Histogram of the recrystallized grain size (red) and subgrains size (blue) distribution in the vein. (h-i) Pole figures of the c-axis orientation of the recrystallized and relic quartz in the mylonite (h) and in the veins (i). Equal area, lower hemisphere projection.

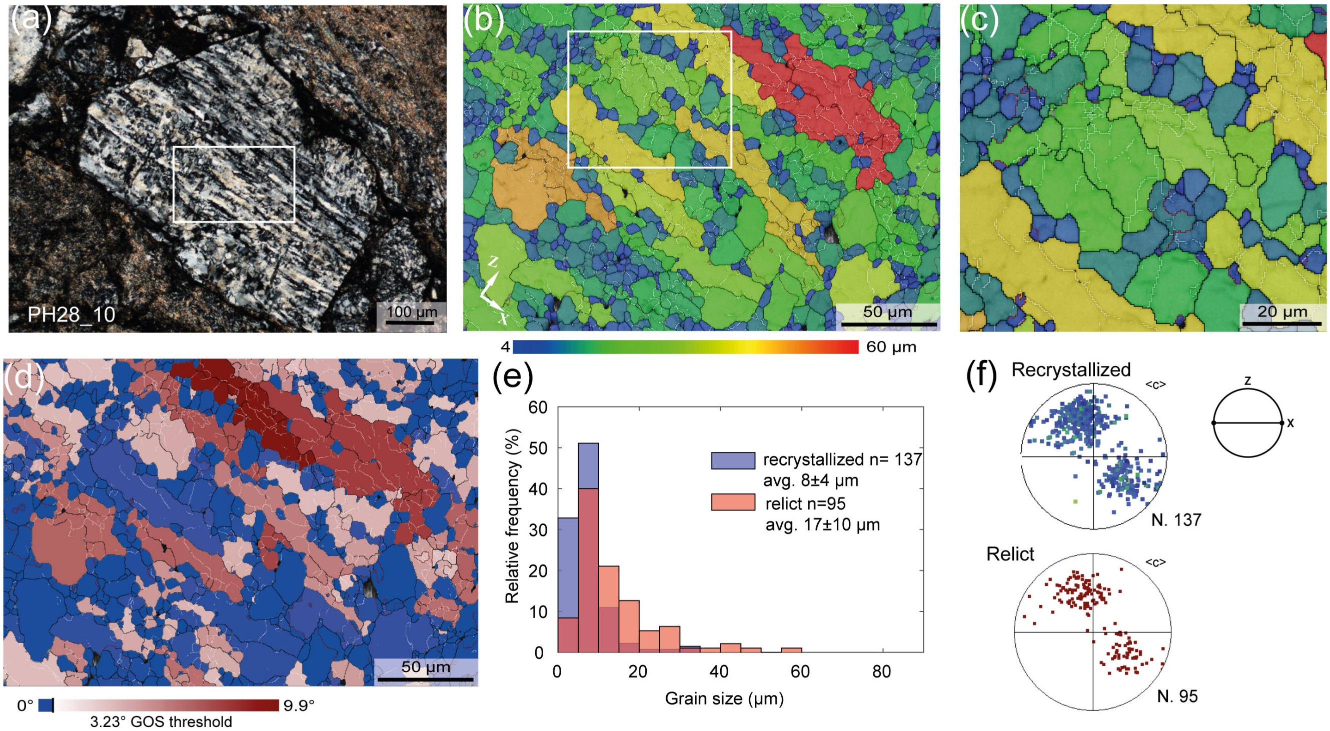

Figure 9. EBSD data of quartz from a clast in the cataclasite. Colour coding of the boundaries like in Figure 6. (a) The analysed quartz clast (Fig. 5f). The white rectangle locates the EBSD map shown in (b-d). (b-c) Grain size map (diameter of the equivalent circle, µm). The map highlights the presence of subgrains in the coarser elongated quartz grains with size comparable to the surrounding finer quartz. (d) GOS map. (e) Histogram of the grain size distribution of the recrystallized (blue) and relict (red) grains. (f) Pole figure of the c-axis orientation of recrystallized and relict grains. Equal area, lower hemisphere projection, color coded as GOS map.

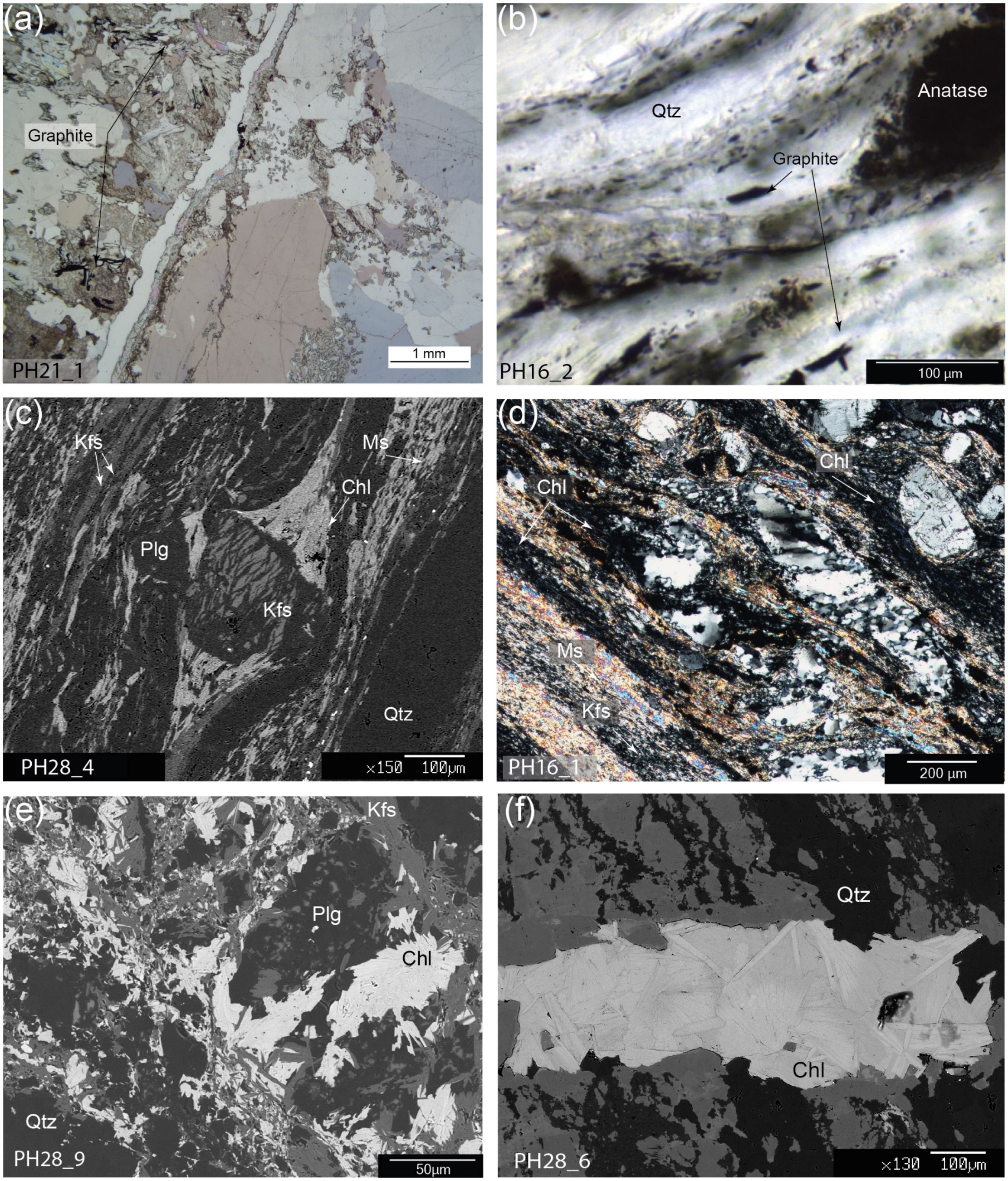

Figure 10. Light microscopy and SEM backscattered electron (BSE) images of characteristic microstructural domains and mineral assemblages used for geothermobarometry estimates. (a) Graphite flakes in association with radiate chlorite in the host rock. Plane polar light. (b) Detail of graphite grains along the mylonitic foliation of BFZ045. Plane polar light. (c) Chlorite in pressure shadows around a K-feldspar porphyroclast in the mylonite. White mica and a fine grained recrystallized K-feldspar assemblage is common along the foliation. (d) Light microscope image of a microstructure similar to (c), cross polar light. (e-f) SEM BSE images of radiate chlorite used for chlorite thermometry in the cataclasite matrix (e) and in a vein cutting the mylonitic foliation (f). The trace of the mylonitic foliation in (f) is oriented ca. NW-SE.

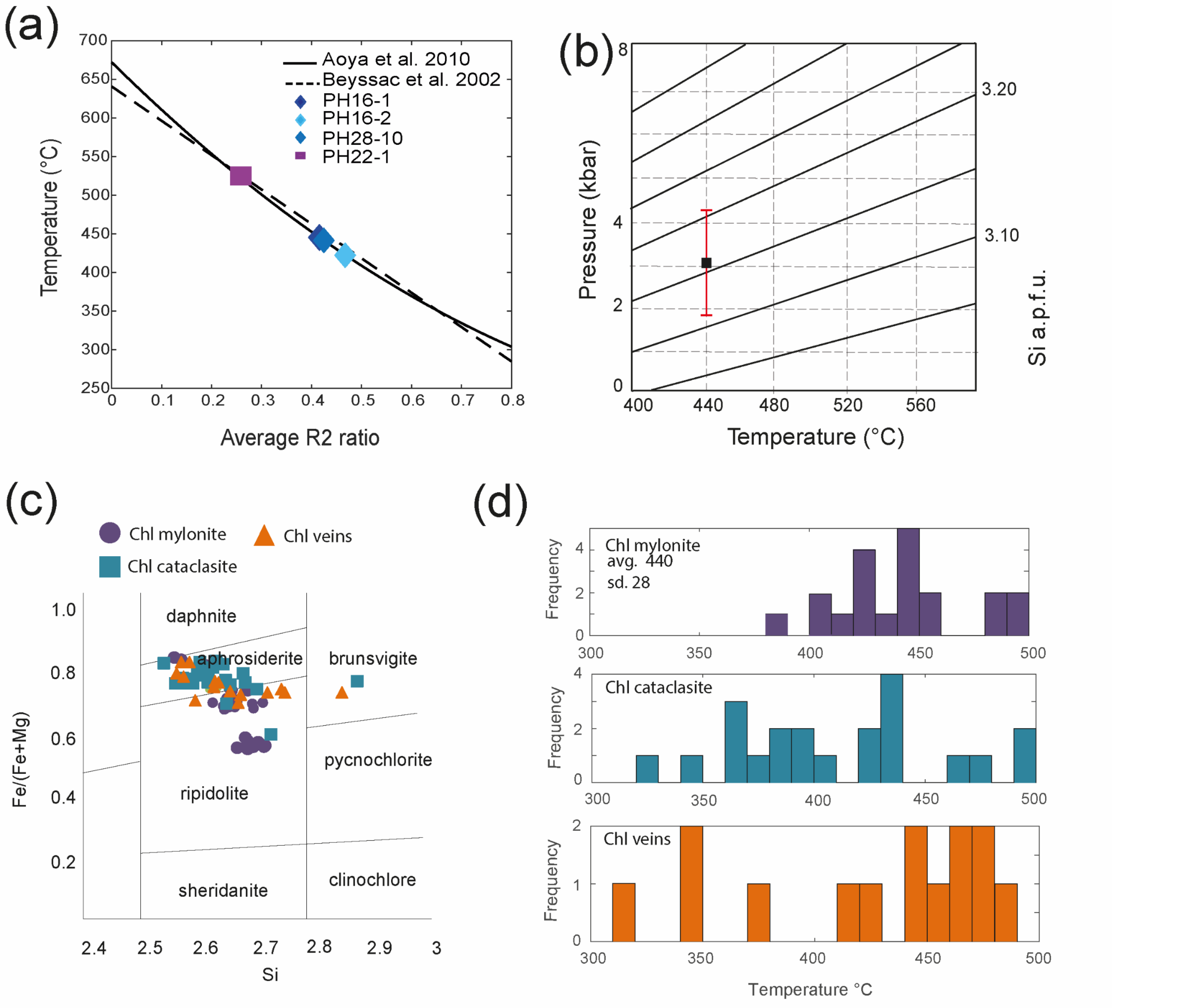

Figure 11. Results of P-T estimates. (a) Carbonaceous material Raman geothermometer. Average R2 ratio (refer to text for explanation) for graphite rich mylonitic and host rock samples was measured to derive a T estimate using the method of Beyssac et al. (2002) and Aoya et al. (2010). (b) Estimated P of mylonitization using the Si-in-phengite barometer (Massonne and Schreyer, 1987) for the average T of 440° C obtained with the carbonaceous material Raman thermometry.Red line show the total spread of the Si values obtained. Black square show the (c) Chlorite compositional diagram based on Hey (1954). (d) Chlorite formation temperature estimated for mylonitic foliation, veins and cataclasite using the method of Lanari et al. (2014).

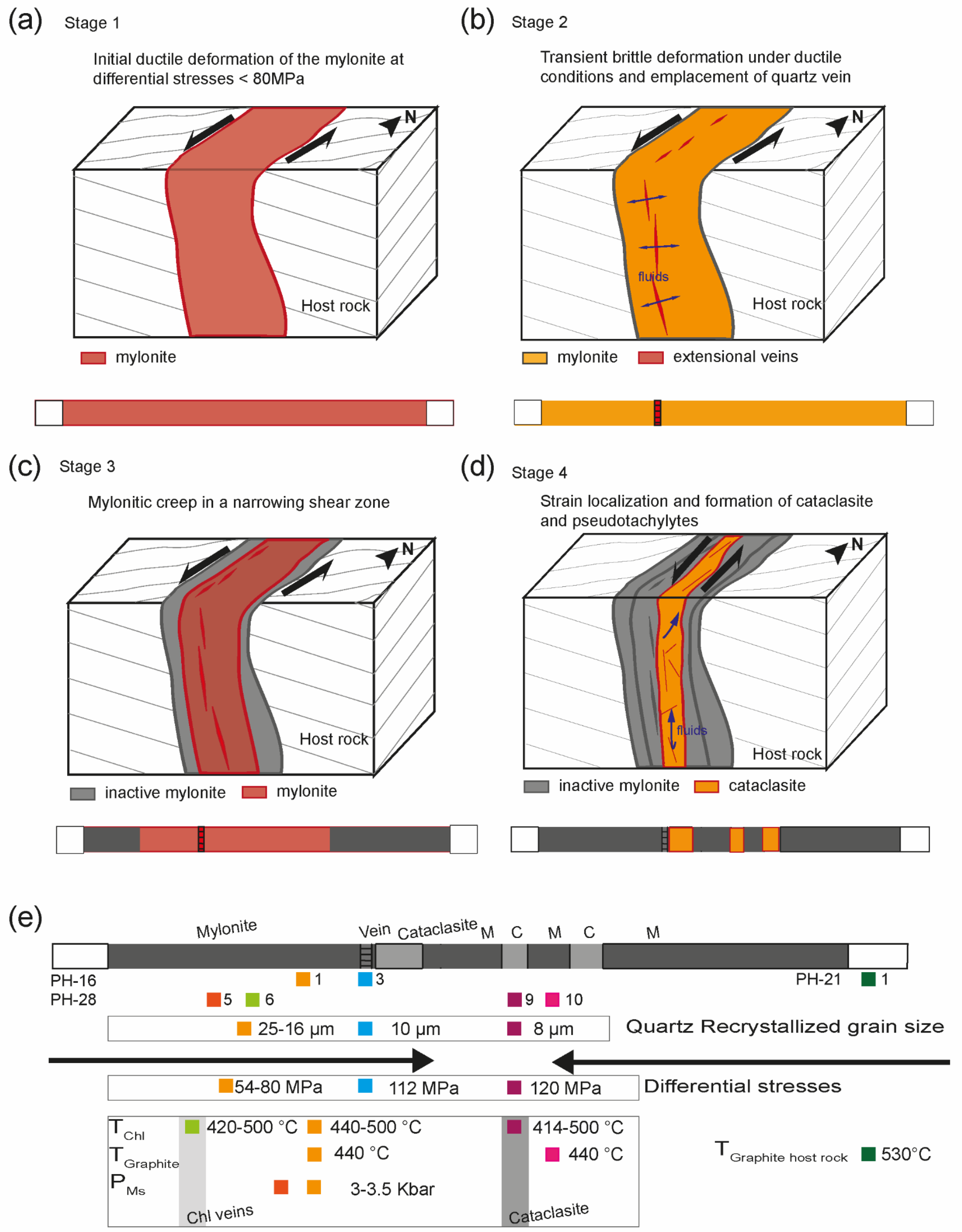

Figure 12. Schematic representation of the microstructural evolution of BFZ045. (a-d) Grey lines: traces of metamorphic foliation in the host rock. In the schematic fault scheme evolution, red displays the active deformation process, grey represents the inactive deformation processes, and orange suggests a transition in the deformation. (a) The development of mylonite was punctuated by the emplacement of quartz vein (b). (c) Ductile deformation localised toward the centre of the mylonitic fault core in an overall narrowing shear zone, and was followed by formation of cataclasite, chlorite veins and pseudotachylyte (d). (e)~~Figure 12.~~ Schematic summary of the quartz recrystallized grain size, differential stresses, and P–T conditions of deformation for BFZ045 derived in the present study, in relationship to the fault core geometry. Each sample is coloured differently to indicate the spatial position of the results described in section 4 of this paper.

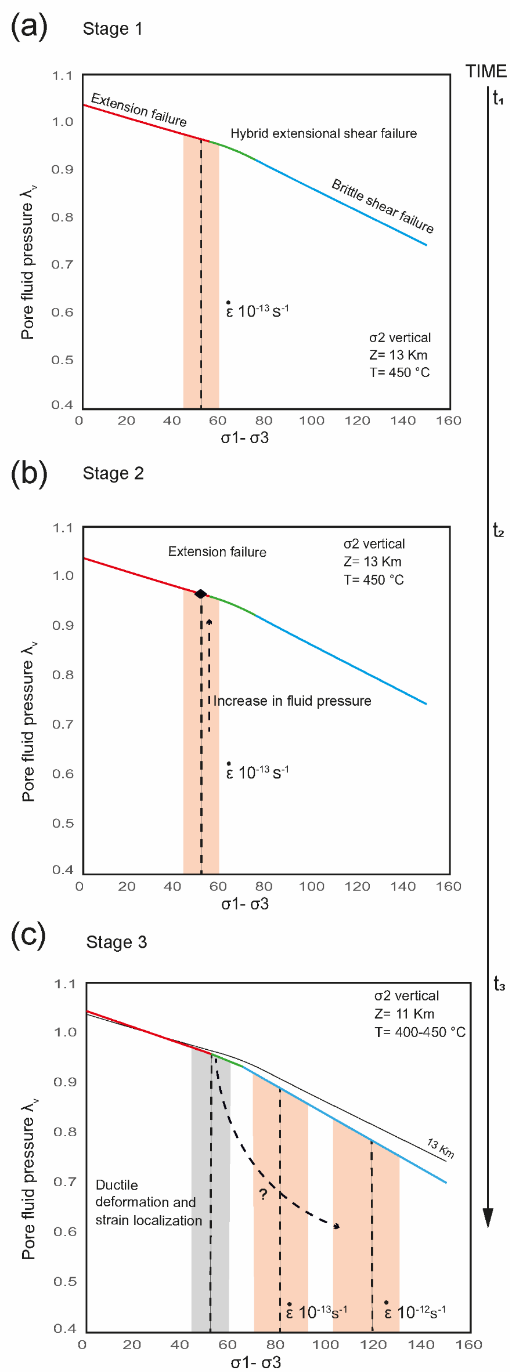

Figure 13. Conceptual model of the temporal and mechanical evolution of the BFZ045 fault zone (see text for more details). BFZ045 was characterized by (a) the development of mylonite ~~under low differential stress~~creeping at ca. 10^{-13} s^{-1}, followed by (b) a transient increase in fluid pressure responsible for the emplacement of quartz ~~vein. (c) Progressive exhumation and cooling resulted in strain~~

~~localization toward the centre of the mylonitic fault core in an overall narrowing shear zone, with subsequent deformation of the fault under brittle condition and associated formation of cataclasite and pseudotachylyte (d).~~veins. Ductile deformation then continued under increasing differential stress and strain rates (c).